5-2016

Kinetic Monte Carlo Models for Crystal Defects

Kyle Louis Golenbiewski
University of Tennessee - Knoxville, kgolenbi@vols.utk.edu

To the Graduate Council:

I am submitting herewith a dissertation written by Kyle Louis Golenbiewski entitled "Kinetic Monte Carlo Models for Crystal Defects." I have examined the final electronic copy of this dissertation for form and content and recommend that it be accepted in partial fulfillment of the requirements for the degree of Doctor of Philosophy, with a major in Mathematics.

Tim P. Schulze, Major Professor

We have read this dissertation and recommend its acceptance:

Yanfei Gao, Henry Simpson, Steven Wise

Accepted for the Council:
Dixie L. Thompson

Vice Provost and Dean of the Graduate School

(Original signatures are on file with official student records.)

Kinetic Monte Carlo Models for Crystal Defects

A Dissertation Presented for the

Doctor of Philosophy

Degree

The University of Tennessee, Knoxville

Kyle Louis Golenbiewski

May 2016

I dedicate this dissertation to my friends and family, without whose unwavering love and support I would not be in the position that I am. I am especially indebted to my parents Mary Alice Golenbiewski and Roy Joseph Golenbiewski for allowing me every opportunity to succeed in life. As this journey comes to a conclusion, another begins. This work is dedicated to my fiancée Nicole Deeann Puckett, whom I am beyond grateful for choosing to share her life with me.

Acknowledgments

First and foremost, I would like to thank my advisor Dr. Tim P. Schulze, without whom this dissertation would not have been possible. His support and encouragement are greatly appreciated, as well as his wealth of knowledge in the field of poker. I would also like to thank Dr. Yanfei Gao, Dr. Henry Simpson, and Dr. Steven Wise for their service on my committee. A special thanks goes to the National Science Foundation for their financial support through the NSF FRG grant DMS-0854870.

I am especially grateful to Dr. Peter Smereka, formerly of the University of Michigan, for several helpful conversations before his unexpected passing this last year. My condolences go out to his friends and family.

This is my simple religion. There is no need for temples; no need for complicated philosophy. Our own brain, our own heart is our temple; the philosophy is kindness.

∼ Tenzin Gyatso, 14th Dalai Lama

Abstract

Kinetic Monte Carlo algorithms have become an increasingly popular means to simulate stochastic processes since their inception in the 1960's. One area of particular interest is their use in simulations of crystal growth and evolution in which atoms are deposited on, or hop between, predefined lattice locations with rates depending on a crystal's configuration. Two such applications are heteroepitaxial thin films and grain boundary migration. Heteroepitaxial growth involves depositing one material onto another with a different lattice spacing. This misfit leads to long-range elastic stresses that affect the behavior of the film. Grain boundary migration, on the other hand, describes how the interface between oriented crystals evolves under a driving force. In ideal grain growth, migration is driven by curvature of the grain boundaries in which the boundaries move towards their center of curvature. This results in a reduction of the total grain boundary surface area of the system, and therefore the total energy of the system. We consider both applications here. Specifically, we extend the analysis of an Energy Localization Approximation applied to Kinetic Monte Carlo simulations of two-dimensional film growth to a three-dimensional setting. We also propose a Kinetic Monte Carlo model for grain boundary migration in the case of arbitrarily oriented face-centered cubic crystals.

Table of Contents

1 Introduction **1**

2 Heteroepitaxial Thin Films **5**

2.1 Introduction 5

2.2 Analysis of Energy Localization in a Three-Dimensional Setting . . . 7

2.2.1 Energy Localization Approximation 11

2.2.2 Proof of Theorems 15

2.3 Summary 26

3 Grain Boundary Migration Driven By Curvature **27**

3.1 Introduction 27

3.2 KMC Model 31

3.2.1 State-space 31

3.2.2 Allowed Transitions 32

3.2.3 Transitional Rates 33

3.3 Limitations 33

3.4 Implementation 34

3.5 Results 38

3.5.1 Parabolic Law 38

3.5.2 Non-parabolic Behavior 40

3.6 Summary 42

4 Summary and Future Directions **45**

Bibliography **47**

Appendix **52**

A Derivation of (2.17) **53**

Vita **59**

List of Figures

2.1 Vertical cross section of an isolated island sitting on an unbounded and otherwise flat film on a flat substrate (gray). 8

2.2 (a) Vertical cross section of the union of the film and substrate (gray), with the truncated domain highlighted in a darker shade of gray. (b) Vertical cross section after the removal of a chunk of material meant to characterize removing an atom in the continuum analogue. 13

3.1 High resolution electron microscopy (HREM) observation of Au island grain shrinkage atop a Ge substrate [19]. 27

3.2 Sample microstructure on a triangular lattice showing the boundaries of five grains represented by spin numbers [26]. 29

3.3 Unit cell of a FCC crystal, where a is the lattice spacing and dotted lines denote nearest neighbors on the faces. Each atom has 12 nearest neighbors and 6 next-nearest neighbors. 30

3.4 Upper-bound on search radius for localized change in nearest neighbor and accessible site counts once a transition has taken place. 37

3.5 Plot of surface area vs. time showing parabolic growth law. 39

3.6 Snapshots of grain evolution showing that the grain maintains a spherical shape and facets during shrinkage. Snapshots were created using the Visual Molecular Dynamics (VMD) program. Only surface atoms are displayed. 39

3.7 Experimental (left) and MD (right) plots of surface area vs. time for cylindrical Au grains showing non-parabolic growth. 40
3.8 Plot of surface area vs. time showing how the parabolic growth law begins to break down. 41
3.9 Plot of surface area vs. time showing non-parabolic growth. 41
3.10 Plot of the difference in inter-grain moves vs. radius for atoms with 6 nearest neighbors on its own lattice. 43

Chapter 1

Introduction

The overarching theme of the work presented here is the use of Kinetic Monte Carlo (KMC) in the simulation of crystal growth and evolution. In Chapter 2, we consider the growth and evolution of a heteroepitaxial thin film. This work focuses on the analysis of an Energy Localization Method first proposed by Schulze and Smereka that is used in KMC simulations of heteroepitaxial growth ([22]-[24]). In Chapter 3, we consider the motion of grain boundaries driven by curvature for arbitrarily oriented face-centered cubic (FCC) crystals. A KMC model for grain boundary migration is introduced and a discussion of numerical results is provided.

While Monte Carlo (MC) generically refers to algorithms designed to solve problems through the use of random numbers, KMC specifically refers to algorithms designed to simulate the evolution of systems dynamically from state to state. At an atomistic level, Molecular Dynamics (MD) simulations are widely used because of their ability to accurately represent a physical system. In MD simulations, a set of initial conditions on the positions and velocities of particles in the system are prescribed, as well as an interaction potential that describes the forces between particles. The evolution of the system in time is then governed by the classical laws of mechanics, which must be solved via integration at every step. A major limitation is that sufficiently small time steps ($\sim 10^{-15}$ s) corresponding to vibrational

frequencies are necessary to accurately integrate the laws of motion [30]. As a result, MD simulations are typically limited to processes that take place on time scales less than a microsecond. In the case of grain boundary migration, experiments have shown that total collapse may occur on the order of seconds [19].

Voter [30] describes an infrequent-event system as a system in which the dynamics is characterized by occasional transitions from one state to another, with long periods of inactivity between transitions. For many solid-state atomic systems, the system spends most of its time randomly oscillating about a local minimizer of the potential energy. After many vibrational periods, the system may overcome an energy barrier and transition from one energy basin to another. Rates can be assigned to each possible escape out of the current basin to an adjacent basin that characterize the probability of transitioning from the current state to an adjacent state. Since the system tends to stay in a particular basin for a long period of time when compared to the time of a vibrational period, the system loses memory of how it got to that state. Hence, the rates do not depend on what states preceded the current state. Then, the state-to-state dynamics correspond to a Markov chain since the transition probabilities depend only on the current configuration and do not consider the steps taken to get there. Since the transition between states depends only on the known rates, a stochastic process can be used in lieu of finding the trajectory of all particles in the system.

One of the benefits of KMC is that rather than following the trajectory of particles through vibrational periods, only diffusive jumps from state to state are considered. As a result, long-time dynamics are achievable on scales much longer than those realized via MD simulations. KMC models typically fall under the umbrella of discrete-space, continuous-time Markov processes in which a system passes through a sequence of states $\{x_{t_k} \in X\}$ drawn from a model dependent state-space X at transition times $\{0 < t_1 < \cdots < t_k < \cdots\}$ [21]. One can view the sequence $\{x_{t_k}\}$ as a Markov chain that is associated with a Poisson process with rate $Q(t)$ that generates a sequence of waiting times $\{\Delta t_k\}$ for periods between transitions. The goal, then,

is to produce samples of these sequences from all possible transitions as efficiently as possible.

We shall now describe a general application of KMC to simulating crystal growth and evolution. We will concern ourselves with only rejection-free algorithms in which all moves sampled from a list of accessible states are accepted. One must first initialize the time $t_0 = 0$ and state x_{t_0} from the model dependent state-space. A common way to represent the state-space is with a set of occupation arrays in which sites are either occupied or unoccupied (typically denoted by 1's and 0's). Next, one must form an ordered list of all possible transitions from the current state and assign rates to these transitions. Once the rates r_{ij} for all transitions from the current state X_i to any state X_j that can be realized are known, one calculates the partial sums

$$S_j = \sum_{k=1}^{j} r_{ik}$$

for $j = 1, \ldots, N_i$, where N_i is the total number of states that can be reached from X_i. Furthermore, one defines

$$Q = \sum_{X_j} r_{ij} = \sum_{k=1}^{N_i} r_{ik}, \tag{1.1}$$

which is the rate for the overall process at the current time step. One then chooses a uniform random number $u \in (0, 1]$ and selects the event J to carry out by finding the J for which $S_{J-1} < uQ \leq S_J$. Once an event is selected, the event is carried out and the state is updated such that $X_i \to X_J$.

The next step is to update the time. This requires knowledge of the cumulative distribution function for the time of first escape from the current state, which is the same as the waiting time. We recall that the k-th arrival time in a Poisson process

with rate λ has the gamma probability density function

$$f^k(t) = \lambda^k \frac{t^{k-1}}{(k-1)!} e^{-\lambda t}$$

for $t \geq 0$. It follows that $f^1(t) = \lambda e^{-\lambda t}$. Let T be the waiting time until the first event occurs. Then, for $t \geq 0$,

$$P(T \leq t) = \int_0^t \lambda e^{-\lambda s} \, ds = 1 - e^{-\lambda t}.$$

As previously mentioned, the rate for the overall process at the current time step is given by (1.1). Hence, $P(T \leq t) = 1 - e^{-Qt}$. One then selects a new uniform random number $u' \in [0, 1)$ and computes the waiting time

$$\Delta t = -\frac{\ln(1 - u')}{Q} = -\frac{\ln(\widetilde{u}')}{Q},$$

where $1 - u' = \widetilde{u}' \in (0, 1]$ is a uniform random number. We note that the same average time scale can be obtained with $\Delta t = 1/Q$ since

$$\int_0^1 \ln(\widetilde{u}') \, d\widetilde{u}' = -1.$$

The time is incremented by Δt and the process is repeated until the evolution of the system is complete.

Chapter 2

Heteroepitaxial Thin Films

2.1 Introduction

This work concerns heteroepitaxial thin films—thin layers of crystalline material that have been deposited on a crystalline substrate. Such films are used in a wide variety of applications, including the fabrication of semiconductors, which has lead to the production of high-brightness light-emitting diodes, lasers, and high-frequency transistors [3]. Since the two species will typically have a lattice mismatch, the behavior of the film is heavily influenced by long-range elastic stresses ([11], [25]).

At the atomistic level, KMC is an effective way of simulating the growth and evolution of such films ([12], [14], [20], [22]-[24]). KMC simulates both a crystal's evolution toward equilibrium and the influence of nonequilibrium processes, such as deposition. It does this via a Markov Chain model, where potential configuration changes are assigned rates. The rates themselves can be deduced from experiments, calculated from energy landscape calculations and transition state theory, or given by empirical models. When elastic forces are absent, a typical model is to assume single-atom moves to neighboring lattice sites with a rate that scales exponentially with the number of nearest neighbors. For an atom i, this rate is

$$r_i = ke^{-\gamma n_i/(k_B T)},$$

where n_i is the total number of nearest neighbor bonds with atom i, γ is the bond energy, k_BT is the thermal energy, and k is a scaling factor. While far from the most accurate approach, these "bond counting" models offer heuristic insight into a system's behavior while being significantly faster and easier to implement than more fundamental approaches. The introduction of elastic interactions into these models substantially increases the complexity of KMC, however, and until recently it was not possible to do three-dimensional simulations on practical length and time scales. One of the key ideas that made these simulations possible was the use of an Energy Localization Approximation ([23],[24]).

Orr et al. [17], Lam et al. [12], and Lung et al. [14] proposed a modification to the simple bond counting model that takes into effect the elastic contribution to the energy of the system that is associated with a displacement field for each configuration. The model that is used for the rates in the particular KMC simulations mentioned above adopts this approach and is a hybrid model that combines a nearest-, next-nearest, and third-nearest neighbor bond-counting scheme with an elastic model based on a network of springs obeying Hooke's law. In terms of the hopping rate, this amounts to an additional term, ΔW, that measures the elastic contribution to the energy barrier when atom i hops:

$$r_i = ke^{-(\gamma n_i + \Delta W)/(k_B T)},$$

where n_i is the sum of nearest-, next-nearest, and third-nearest neighbor bonds. The elastic contribution to the energy barrier is modeled as the difference in the total elastic energy with and without the atom for which the rate is being calculated. If one were to fully implement this model, it would involve a prohibitively high computational complexity.

The essence of the Energy Localization Approximation is to do a local calculation centered on the atom in question. Intuitively, it seems that this might be promising, as we are only changing the network of interacting springs at a single lattice site.

Nevertheless, elastic forces are notoriously long-ranged, with Green's tensors that decay like one over distance. So it is somewhat surprising that the accuracy of this method turns out to scale significantly better than this. Schulze and Smereka [22] were able to show that for the case of a substrate occupying the entire half-plane $y < 0$ that is completely covered by a small-amplitude film of uniform height outside some radius R, the error between the exact energy barrier and localization approximation scales like one over the distance squared. This assessment is made by analyzing the analogous problem in the context of linear elasticity, where a small-slope approximation resulting from assumptions on the small-amplitude film plays a key role in determining the scaling behavior. It is shown through the analysis that this scaling is due to a fortunate cancellation of boundary terms in what would otherwise be the largest contributor to the error. A more intuitive approach in which a simple truncation of the energy integrals using exact displacement fields was considered as well. They showed that the error for this truncation approximation decays much slower and scales like one over the distance. Furthermore, the error scales linearly with the thickness of the film. The work in this dissertation is specifically concerned with characterizing the accuracy of the localization approximation, extending the work of Schulze and Smereka to a three-dimensional setting.

2.2 Analysis of Energy Localization in a Three-Dimensional Setting

For the theorems that follow, we consider a system in which a substrate occupying the entire half-space $z < 0$ is completely covered by a small-amplitude film $0 \leq z \leq h(x, y)$ of uniform height H for $x^2 + y^2 > R^2$ (see Figure 2.1). The displacement of the film, $\mathbf{u}$, is measured relative to a reference configuration where a flat film sitting atop the substrate is in mechanical equilibrium. With this choice, it can be shown that the

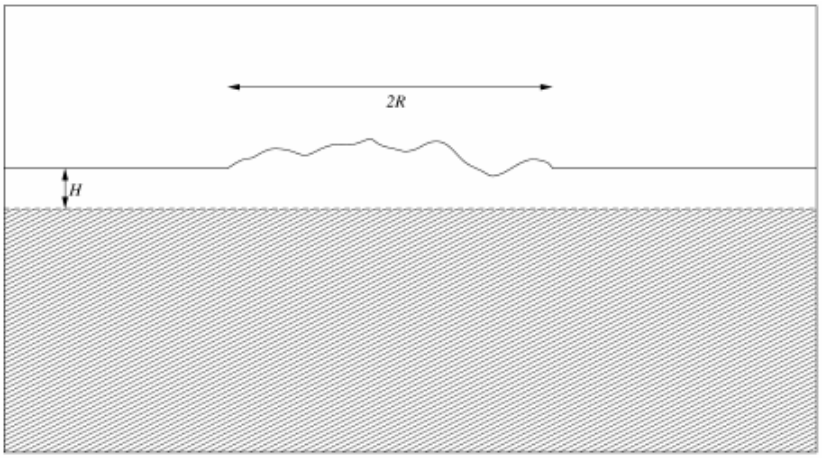

Figure 2.1: Vertical cross section of an isolated island sitting on an unbounded and otherwise flat film on a flat substrate (gray).

vertical lattice spacing, a_L, of the film in equilibrium is

$$a_L = a_f + a_s \alpha_1 \frac{2\lambda}{\lambda + 2\mu}, \tag{2.1}$$

where a_f is the natural lattice spacing of the film, a_s is the lattice spacing of the substrate, α_1 is the scaled misfit given below, and λ and μ are the Lamé constants [20].

Appealing to linear elasticity theory, the elastic energy density of an isotropic material is given by

$$w = \frac{1}{2}\left(\lambda + \frac{2}{3}\mu\right)\left(\sum_{k=1}^{3} E_{kk}\right)^2 + \mu \sum_{i,j=1}^{3}\left(E_{ij} - \frac{1}{3}\delta_{ij}\sum_{k=1}^{3} E_{kk}\right)^2,$$

where $\mathbf{E}$ is the strain tensor defined as the sum of an intrinsic, or stress-free, strain $\overline{\mathbf{E}}$ and a relative strain $\widetilde{\mathbf{E}}$ [5]. Here, we have

$$E_{ij} = \overline{E}_{ij} + \widetilde{E}_{ij},$$

where

$$\widetilde{E}_{ij} = \frac{1}{2}(\partial_i u_j + \partial_j u_i) \quad \text{and} \quad \overline{\mathbf{E}} = \begin{pmatrix} -\alpha_1 & 0 & 0 \\ 0 & -\alpha_1 & 0 \\ 0 & 0 & -\alpha_2 \end{pmatrix} \theta(z);$$

and we use the strain parameters

$$\alpha_1 = \frac{a_f - a_s}{a_s} \quad \text{and} \quad \alpha_2 = \frac{a_f - a_L}{a_s},$$

and the Heaviside function

$$\theta(z) = \begin{cases} 0 & \text{if } z < 0, \\ 1 & \text{if } z > 0. \end{cases}$$

The diagonal entries of $\mathbf{E}$ correspond to extensional strains [27]. Namely, E_{ii} measures the relative elongation of the lattice spacing of the film with respect to the lattice spacing of the substrate parallel to the x_i-coordinate axis. We see from the strain parameters that if the film has a larger lattice parameter than the substrate, then the epitaxial film is in compressive strain as a result of the misfit. The off-diagonal entires, E_{ij}, correspond to shearing strains that measure the increase in the angle between two adjacent bonds parallel to the x_i- and x_j-coordinate axes [6]. We note that there are no shearing strains that result from the misfit. Then, expanded out, the energy density is

$$\begin{aligned} w \;=\; & \left(\frac{\lambda}{2} + \mu\right)\left[(\partial_1 u_1)^2 + (\partial_2 u_2)^2 + (\partial_3 u_3)^2\right] \\ & + \lambda\left[(\partial_1 u_1)(\partial_2 u_2) + (\partial_1 u_1)(\partial_3 u_3) + (\partial_2 u_2)(\partial_3 u_3)\right] \\ & + \frac{\mu}{2}\left[(\partial_1 u_2)^2 + (\partial_2 u_1)^2 + (\partial_1 u_3)^2 + (\partial_3 u_1)^2 + (\partial_2 u_3)^2 + (\partial_3 u_2)^2\right] \\ & + \mu\left[(\partial_1 u_2)(\partial_2 u_1) + (\partial_1 u_3)(\partial_3 u_1) + (\partial_2 u_3)(\partial_3 u_2)\right] \\ & - \lambda\left(2\alpha_1 + \alpha_2\right)\left[\partial_1 u_1 + \partial_2 u_2 + \partial_3 u_3\right]\theta(z) - 2\mu\left[\alpha_1(\partial_1 u_1 + \partial_2 u_2) + \alpha_2 \partial_3 u_3\right]\theta(z) \\ & + \left[\frac{\lambda}{2}(2\alpha_1 + \alpha_2)^2 + \mu(2\alpha_1^2 + \alpha_2^2)\right]\theta(z). \end{aligned}$$

We note that the stress tensor, $\mathbf{T}$, is defined through

$$T_{ij} = \frac{\partial w}{\partial_j u_i}.$$

Like the strain tensor, the stress tensor can be written as the sum of an intrinsic stress $\overline{\mathbf{T}}$ and a relative stress $\widetilde{\mathbf{T}}$. Namely,

$$T_{ij} = \overline{T}_{ij} + \widetilde{T}_{ij},$$

where

$$\widetilde{T}_{ij} = 2\mu\widetilde{E}_{ij} + \lambda\delta_{ij}\widetilde{E}_{kk} \tag{2.2}$$

and

$$\overline{\mathbf{T}} = \begin{pmatrix} -\sigma_1 & 0 & 0 \\ 0 & -\sigma_1 & 0 \\ 0 & 0 & -\sigma_2 \end{pmatrix} \theta(z), \tag{2.3}$$

where

$$\begin{aligned} \sigma_1 &= 2\left(\lambda+\mu\right)\alpha_1 + \lambda\alpha_2, \\ \sigma_2 &= \left(\lambda+2\mu\right)\alpha_2 + 2\lambda\alpha_1. \end{aligned} \tag{2.4}$$

We point out the use of the Einstein summation convention used in (2.2) where a subscript appearing twice (k in this case) is summed from 1 to 3. The energy density can then be written as

$$\begin{aligned} w \;=\; & \sum_{i,j=1}^{3}\left[\frac{\mu}{2}(\partial_i u_j)(\partial_i u_j + \partial_j u_i) + \frac{\lambda}{2}(\partial_i u_i)(\partial_j u_j) + \overline{T}_{ij}\partial_i u_j\right] \\ & + \left[\alpha_1\sigma_1 + \frac{\alpha_2}{2}\sigma_2\right]\theta(z). \end{aligned} \tag{2.5}$$

Noting that

$$T_{ij} = 2\mu E_{ij} + \lambda\delta_{ij}E_{kk},$$

the energy density can be compactly written as

$$w = \frac{1}{2} \sum_{i,j=1}^{3} E_{ij} T_{ij}.$$

We denote the union of the film and substrate by Ω. The boundary between the film and vacuum is denoted by $\partial\Omega$. Then, the equations of equilibrium maintain that for $i \in \{1, 2, 3\}$,

$$\sum_{j=1}^{3} \partial_j T_{ij} = 0 \quad \text{for } \mathbf{x} \in \Omega,$$
$$\sum_{j=1}^{3} T_{ij} n_j = 0 \quad \text{for } \mathbf{x} \in \partial\Omega.$$

As Schulze and Smereka [22] originally pointed out, the film/substrate interface may introduce a singularity in the first equation due to the stress-free strain. Namely, $\overline{T}_{33}$ has a jump discontinuity at the interface between the film and substrate provided that $\sigma_2 \neq 0$. However, it follows from (2.4), the strain parameters, and (2.1) that $\sigma_2 = 0$. Written more conveniently in vector notation, we then obtain

$$\mu \Delta \mathbf{u} + (\lambda + \mu) \nabla (\nabla \cdot \mathbf{u}) = \mathbf{0} \quad \text{for } \mathbf{x} \in \Omega, \tag{2.6}$$
$$\widetilde{\mathbf{T}} \mathbf{n} = -\overline{\mathbf{T}} \mathbf{n} \quad \text{for } \mathbf{x} \in \partial\Omega, \tag{2.7}$$
$$\mathbf{u} \to \mathbf{0} \quad \text{as } |\mathbf{x}| \to \infty. \tag{2.8}$$

2.2.1 Energy Localization Approximation

We recall that the focus of Schulze and Smereka was on the ability to efficiently approximate the elastic correction to the energy barrier, denoted ΔW, when transitioning from one state to another. Their model (adopted from [12], [14], and

[17]) for this was

$$\Delta W = W(\text{with atom } i) - W(\text{without atom } i),$$

where W is the total elastic energy stored in the configuration. Here, we extend their results by showing that the Energy Localization Approximation scales with the increase in dimension. While the model is applied to discrete simulations in practice, the utility of this approximation is shown using the continuum limit of the discrete model.

The total elastic energy stored in an arbitrary configuration is the integral of the energy density over the domain. Namely, for a displacement field $\mathbf{u}$ satisfying (2.6)-(2.8),

$$W(\mathbf{u}; \Omega) = \int_{\Omega} w \, d\mathbf{x}. \tag{2.9}$$

In practice, this is not feasible to calculate. Rather, we consider approximations to the total elastic energy over finite regions $\Omega_\rho \subset \Omega$. Let $\Omega_\rho = \{\Omega \cap \{|\mathbf{x}| < \rho\}\}$. Then, the elastic correction over an unbounded domain is

$$\Delta W = \lim_{\rho \to \infty} \left[W(\mathbf{u}; \Omega_\rho) - W(\mathbf{u}^m; \Omega_\rho^m) \right], \tag{2.10}$$

where Ω_ρ^m is the same domain except that it has been modified locally and $\mathbf{u}^m$ is the corresponding displacement field (see Figure 2.2).

For the Energy Localization Approximation, we constrain the solution on the modified domain ($\mathbf{u}_L^m$) to agree with the solution on the original domain along the boundary of the truncated domain below the surface. Namely,

$$\mathbf{u}_L^m = \mathbf{u} \quad \text{for } \mathbf{x} \in \Gamma_\rho.$$

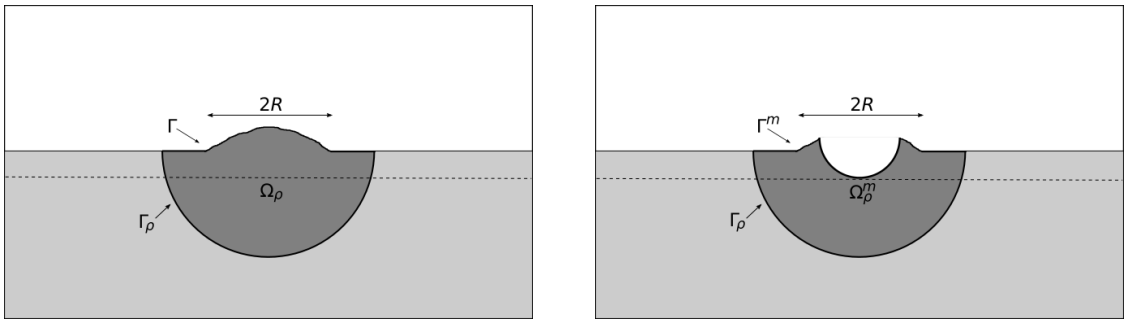

(a) Original Domain **(b)** Modified Domain

Figure 2.2: (a) Vertical cross section of the union of the film and substrate (gray), with the truncated domain highlighted in a darker shade of gray. (b) Vertical cross section after the removal of a chunk of material meant to characterize removing an atom in the continuum analogue.

Then, the approximation to the displacement field on the modified domain is

$$\mathbf{u}_L^m = \begin{cases} \mathbf{u}_L^m & \text{if } |\mathbf{x}| < \rho, \\ \mathbf{u} & \text{if } |\mathbf{x}| = \rho. \end{cases}$$

The corresponding Energy Localization Approximation to the elastic correction to the energy barrier is

$$\Delta W_L = W(\mathbf{u}; \Omega_\rho) - W(\mathbf{u}_L^m; \Omega_\rho^m), \tag{2.11}$$

which leads us to our first theorem.

THEOREM 1 - Energy Localization Approximation. *Suppose that $h(x, y)$ is a compactly supported function whose support includes $(0, 0)$. Further, suppose that $h(x, y)$ is modified by a localized change centered at $(0, 0)$. Then,*

$$\Delta W - \Delta W_L = O(\epsilon/\rho^3) \quad as \quad \rho \to \infty,$$

where ΔW and ΔW_L are defined by (2.10) and (2.11) respectively, and ϵ is a small parameter that characterizes the film profile.

We recall that the original result in the two-dimensional setting showed that the error scales like one over the distance squared [22]. As we see, the error here scales by an additional factor of $1/\rho$ when compared to the original two-dimensional result. To gain more appreciation for the Energy Localization Approximation, Schulze and Smereka compared this result with that of an Energy Truncation Approximation. For the truncated approximation, they integrated the *exact* displacement field on the modified domain over the same truncated domain. Then, the Energy Truncation Approximation to the elastic correction to the energy barrier is

$$\Delta W_T = W(\mathbf{u}; \Omega_\rho) - W(\mathbf{u}^m; \Omega_\rho^m). \tag{2.12}$$

While this may intuitively seem like a better approximation, they showed that this was not the case. Furthermore, in contrast to Theorem 1, the result for the Energy Truncation Approximation does not scale with dimension. Namely,

THEOREM 2 - Nonlocality of the Energy Density. *Under the same hypotheses of Theorem 1,*

$$\Delta W - \Delta W_T = O(\epsilon H/\rho) \quad as \quad \rho \to \infty,$$

where ΔW and ΔW_T are defined by (2.10) and (2.12) respectively.

This result is the same as in the two-dimensional setting and further demonstrates the utility of the Energy Localization Approximation as a means of computing the elastic correction to the energy barrier. We prove each of these results in the next section.

2.2.2 Proof of Theorems

Let $\mathbf{u}$ be a displacement field satisfying (2.6)-(2.8). We begin by noting that (2.5) can be written in vector notation as

$$w = \mu\left(\nabla\cdot\widetilde{\mathbf{E}}\mathbf{u} - \mathbf{u}\cdot\left(\nabla\cdot\widetilde{\mathbf{E}}\right)\right) + \frac{\lambda}{2}\left(\nabla\cdot\mathbf{u}\right)^2 + \nabla\cdot\overline{\mathbf{T}}\mathbf{u} + \alpha_1\sigma_1\theta(z).$$

Furthermore,

$$\nabla\cdot\widetilde{\mathbf{E}} = \frac{1}{2}\left(\Delta\mathbf{u} + \nabla(\nabla\cdot\mathbf{u})\right)$$

and

$$\left(\nabla\cdot\mathbf{u}\right)^2 = \nabla\cdot(\nabla\cdot\mathbf{u})\mathbf{u} - \mathbf{u}\cdot\nabla(\nabla\cdot\mathbf{u}).$$

Then, recalling (2.2) and (2.6), the elastic energy density can be written in divergence form as

$$\begin{aligned} w &= \nabla\cdot\left(\mu\widetilde{\mathbf{E}}\mathbf{u} + \frac{\lambda}{2}(\nabla\cdot\mathbf{u})\mathbf{u} + \overline{\mathbf{T}}\mathbf{u}\right) - \frac{1}{2}\mathbf{u}\cdot\left(\mu\Delta\mathbf{u} + (\lambda+\mu)\nabla(\nabla\cdot\mathbf{u})\right) + \alpha_1\sigma_1\theta(z) \\ &= \nabla\cdot\left(\mu\widetilde{\mathbf{E}}\mathbf{u} + \frac{\lambda}{2}(\nabla\cdot\mathbf{u})\mathbf{u} + \overline{\mathbf{T}}\mathbf{u}\right) + \alpha_1\sigma_1\theta(z) \\ &= \nabla\cdot\left(\frac{1}{2}\widetilde{\mathbf{T}}\mathbf{u} + \overline{\mathbf{T}}\mathbf{u}\right) + \alpha_1\sigma_1\theta(z). \end{aligned}$$

Inserting the above divergence form into (2.9) on a finite subdomain $\Omega_\rho \subseteq \Omega$, the total elastic energy can be written as a boundary integral:

$$W(\mathbf{u};\Omega_\rho) = \int_{\partial\Omega_\rho}\left(\frac{1}{2}\widetilde{\mathbf{T}}\mathbf{u} + \overline{\mathbf{T}}\mathbf{u}\right)\cdot\mathbf{n}\,dS + \alpha_1\sigma_1|\Omega_f\cap\Omega_\rho|,$$

where Ω_f denotes the film. Similarly,

$$W(\mathbf{u}^m;\Omega_\rho^m) = \int_{\partial\Omega_\rho^m}\left(\frac{1}{2}\widetilde{\mathbf{T}}^m\mathbf{u}^m + \overline{\mathbf{T}}\mathbf{u}^m\right)\cdot\mathbf{n}\,dS + \alpha_1\sigma_1|\Omega_f^m\cap\Omega_\rho^m|.$$

Recalling (2.7) and taking the limit as $\rho \to \infty$, (2.10) gives the exact correction to the energy barrier:

$$\Delta W = \frac{1}{2}\int_{\partial\Omega} \mathbf{u}\cdot\overline{\mathbf{T}}\mathbf{n}\,dS - \frac{1}{2}\int_{\partial\Omega^m} \mathbf{u}^m\cdot\overline{\mathbf{T}}\mathbf{n}\,dS + \alpha_1\sigma_1|\Omega\backslash\Omega^m|.$$

Likewise, using (2.11) and (2.12), we find the Energy Localization Approximation and Energy Truncation Approximation, respectively, of the correction to the energy barrier:

$$\begin{aligned}
\Delta W_L &= \frac{1}{2}\int_{\Gamma} \mathbf{u}\cdot\overline{\mathbf{T}}\mathbf{n}\,dS - \frac{1}{2}\int_{\Gamma^m} \mathbf{u}_L^m\cdot\overline{\mathbf{T}}\mathbf{n}\,dS + \alpha_1\sigma_1|\Omega\backslash\Omega^m| + \\
&\quad \frac{1}{2}\int_{\Gamma_\rho} \mathbf{u}\cdot\left(\widetilde{\mathbf{T}} - \widetilde{\mathbf{T}}_L^m\right)\mathbf{n}\,dS, \\
\Delta W_T &= \frac{1}{2}\int_{\Gamma} \mathbf{u}\cdot\overline{\mathbf{T}}\mathbf{n}\,dS - \frac{1}{2}\int_{\Gamma^m} \mathbf{u}^m\cdot\overline{\mathbf{T}}\mathbf{n}\,dS + \alpha_1\sigma_1|\Omega\backslash\Omega^m| + \\
&\quad \frac{1}{2}\int_{\Gamma_\rho} \left(\mathbf{u}\cdot\widetilde{\mathbf{T}} - \mathbf{u}^m\cdot\widetilde{\mathbf{T}}^m\right)\mathbf{n}\,dS + \int_{\Gamma_\rho}(\mathbf{u}-\mathbf{u}^m)\cdot\overline{\mathbf{T}}\mathbf{n}\,dS,
\end{aligned}$$

where the boundaries $\partial\Omega_\rho = \Gamma\cup\Gamma_\rho$ and $\partial\Omega_\rho^m = \Gamma^m\cup\Gamma_\rho$ have been decomposed into surface and subsurface components (see Figure 2.2). The corresponding errors of each approximation are then:

$$\begin{aligned}
E_L &= \frac{1}{2}\int_{\partial\Omega\backslash\Gamma} \mathbf{u}\cdot\overline{\mathbf{T}}\mathbf{n}\,dS - \frac{1}{2}\int_{\partial\Omega^m\backslash\Gamma^m} \mathbf{u}^m\cdot\overline{\mathbf{T}}\mathbf{n}\,dS + \\
&\quad \frac{1}{2}\int_{\Gamma^m}(\mathbf{u}_L^m-\mathbf{u}^m)\cdot\overline{\mathbf{T}}\mathbf{n}\,dS - \frac{1}{2}\int_{\Gamma_\rho} \mathbf{u}\cdot\left(\widetilde{\mathbf{T}} - \widetilde{\mathbf{T}}_L^m\right)\mathbf{n}\,dS, \qquad (2.13)
\end{aligned}$$

and

$$\begin{aligned}
E_T &= \frac{1}{2}\int_{\partial\Omega\backslash\Gamma} \mathbf{u}\cdot\overline{\mathbf{T}}\mathbf{n}\,dS - \frac{1}{2}\int_{\partial\Omega^m\backslash\Gamma^m} \mathbf{u}^m\cdot\overline{\mathbf{T}}\mathbf{n}\,dS + \\
&\quad \int_{\Gamma_\rho}(\mathbf{u}^m-\mathbf{u})\cdot\overline{\mathbf{T}}\mathbf{n}\,dS - \frac{1}{2}\int_{\Gamma_\rho} \left(\mathbf{u}\cdot\widetilde{\mathbf{T}} - \mathbf{u}^m\cdot\widetilde{\mathbf{T}}^m\right)\mathbf{n}\,dS. \qquad (2.14)
\end{aligned}$$

Approximate Evaluation of Error Formulas

In order to compare the two approximations, we aim to find asymptotic expressions for the errors given by (2.13) and (2.14) in terms of $1/\rho$. As a reminder, we take a film profile $H + h(x, y)$, where $h(x, y) = 0$ for $x^2 + y^2 > R^2$. In addition, we take h, h_x, and h_y to be $O(\epsilon)$ for $x^2 + y^2 < R^2$. We note that the normal along the surface of the film is

$$\mathbf{n} = \frac{(-h_x(x,y), -h_y(x,y), 1)^T}{\sqrt{1 + h_x^2(x,y) + h_y^2(x,y)}} \sim \mathbf{e}_3 - h_x(x,y)\mathbf{e}_1 - h_y(x,y)\mathbf{e}_2.$$

Then, to leading order, $\mathbf{n} \sim \mathbf{e}_3$. Hence, we approximate the film/vacuum interface as flat when applying the boundary conditions given in (2.7). At this point, it is convenient to translate the film/substrate medium such that the film/vacuum interface is at $z = 0$. Then, it follows from (2.3) that

$$\overline{\mathbf{T}} = \begin{pmatrix} -\sigma_1 & 0 & 0 \\ 0 & -\sigma_1 & 0 \\ 0 & 0 & 0 \end{pmatrix} \theta(z + H). \tag{2.15}$$

Furthermore, it follows from the boundary condition (2.7) that

$$\widetilde{\mathbf{T}}\mathbf{e}_3 = -\sigma_1 \left(h_x(x,y)\mathbf{e}_1 + h_y(x,y)\mathbf{e}_2\right) \quad \text{at } z = 0.$$

The resulting problem for the half-space is then

$$\begin{aligned} \mu\Delta\mathbf{u} + (\lambda + \mu)\nabla\left(\nabla \cdot \mathbf{u}\right) &= \mathbf{0} \quad \text{for } z < 0, \\ \widetilde{\mathbf{T}}\mathbf{e}_3 &= -\sigma_1 \left(h_x(x,y)\mathbf{e}_1 + h_y(x,y)\mathbf{e}_2\right) \quad \text{at } z = 0, \\ \mathbf{u} &\to \mathbf{0} \quad \text{as } |\mathbf{x}| \to \infty. \end{aligned} \tag{2.16}$$

The solution to the above half-space problem can be obtained by following the derivation by Landau and Lifshitz [13]:

$$\mathbf{u} = \sigma_1 \int \int_{x'^2+y'^2 \le R^2} \mathbf{f}(x-x', y-y', z) h(x', y')\, dx' dy' \tag{2.17}$$

where

$$\mathbf{f} = \frac{1}{4\pi\mu} \begin{bmatrix} \frac{x}{r^3}\left(\frac{\lambda+2\mu}{\lambda+\mu} - \frac{3z^2}{r^2}\right) \\ \frac{y}{r^3}\left(\frac{\lambda+2\mu}{\lambda+\mu} - \frac{3z^2}{r^2}\right) \\ \frac{z}{r^3}\left(\frac{\lambda}{\lambda+\mu} - \frac{3z^2}{r^2}\right) \end{bmatrix} = \frac{\partial}{\partial x}\mathbf{G}\mathbf{e}_1 + \frac{\partial}{\partial y}\mathbf{G}\mathbf{e}_2,$$

$r = \sqrt{x^2+y^2+z^2}$, and $\mathbf{G}$ is the Green's tensor (see Appendix A) for

$$\begin{aligned} \mu\Delta\mathbf{u} + (\lambda+\mu)\nabla(\nabla\cdot\mathbf{u}) &= \mathbf{0} \quad \text{for } z<0, \\ \widetilde{\mathbf{T}}\mathbf{e}_3 &= -\sigma_1(h_x(x,y)\delta(x,y)\mathbf{e}_1 + h_y(x,y)\delta(x,y)\mathbf{e}_2) \quad \text{at } z=0, \\ \mathbf{u} &\to \mathbf{0} \quad \text{as } |\mathbf{x}| \to \infty. \end{aligned}$$

Similarly, we obtain $\mathbf{u}^m$ with $h(x,y)$ replaced by $h^m(x,y)$.

At this point, we aim to derive asymptotic expressions for each of the integrals appearing in (2.13) and (2.14). Namely, we show that

$$I_1 = \frac{1}{2}\int_{\partial\Omega\setminus\Gamma} \mathbf{u}\cdot\overline{\mathbf{T}}\mathbf{n}\, dS = 0,$$

$$I_2 = \frac{1}{2}\int_{\partial\Omega^m\setminus\Gamma^m} \mathbf{u}^m\cdot\overline{\mathbf{T}}\mathbf{n}\, dS = 0,$$

$$I_3 = \frac{1}{2}\int_{\Gamma_\rho} (\mathbf{u}\cdot\widetilde{\mathbf{T}} - \mathbf{u}^m\cdot\widetilde{\mathbf{T}}^m)\mathbf{n}\, dS = O(\epsilon^2/\rho^3), \tag{2.18}$$

$$I_4 = \int_{\Gamma_\rho} (\mathbf{u}^m - \mathbf{u})\cdot\overline{\mathbf{T}}\mathbf{n}\, dS = O(\epsilon H/\rho), \tag{2.19}$$

$$I_5 = \frac{1}{2}\int_{\Gamma_\rho} \mathbf{u}\cdot(\widetilde{\mathbf{T}} - \widetilde{\mathbf{T}}^m_L)\mathbf{n}\, dS = O(\epsilon^2/\rho^3), \tag{2.20}$$

and

$$I_6 = \frac{1}{2}\int_{\Gamma^m} (\mathbf{u}_L^m - \mathbf{u}^m)\cdot \overline{\mathbf{T}}\mathbf{n}\, dS = O(\epsilon/\rho^3). \tag{2.21}$$

We recall that the film/vacuum interface is flat for $|\mathbf{x}| > R$. Hence, for $\rho > R$, $I_1 = I_2 = 0$ since $\overline{\mathbf{T}}\mathbf{n} = \mathbf{0}$ (owing to $\sigma_2 = 0$). Using this fact, and equations (2.18) and (2.19), we establish Theorem 2:

$$E_T = O(\epsilon H/\rho).$$

It follows from equations (2.20) and (2.21) that

$$E_L = O(\epsilon/\rho^3),$$

which establishes Theorem 1.

Derivation of Error Estimates

In this section, we establish the estimates provided in the previous section.

Proof of Eq. 2.18. Recall that

$$I_3 = \frac{1}{2}\int_{\Gamma_\rho} (\mathbf{u}\cdot\widetilde{\mathbf{T}} - \mathbf{u}^m\cdot\widetilde{\mathbf{T}}^m)\mathbf{n}\, dS.$$

Furthermore, we recall (2.17) and its analogue

$$\mathbf{u}^m = \sigma_1 \int\int_{x'^2+y'^2\le R^2} \mathbf{f}(x-x', y-y', z)h^m(x', y')\; dx'dy'.$$

We need to evaluate $\mathbf{u}$ and $\widetilde{\mathbf{T}}$ on the lower hemisphere of radius ρ centered at $\mathbf{x} = (0,0,0)$. We begin by converting each of the integrals to polar coordinates:

$$\mathbf{u} = \sigma_1 \int_0^{2\pi}\int_0^R \mathbf{f}(x - s\cos\beta, y - s\sin\beta, z)h(s\cos\beta, s\sin\beta)s\; dsd\beta$$

and

$$\mathbf{u}^m = \sigma_1 \int_0^{2\pi} \int_0^R \mathbf{f}(x - s\cos\beta, y - s\sin\beta, z) h^m(s\cos\beta, s\sin\beta) s \; ds d\beta.$$

Let $(x, y, z) = \rho(\sin\varphi\cos\theta, \sin\varphi\sin\theta, \cos\varphi)$ and substitute this into the integrals above. Then, by writing the integrand as a Taylor series in s and expanding in terms of $1/\rho$, we obtain

$$\mathbf{u}\,\big|_{|\mathbf{x}|=\rho} = O(\epsilon/\rho^2) \quad \text{and} \quad \mathbf{u}^m\,\big|_{|\mathbf{x}|=\rho} = O(\epsilon/\rho^2), \tag{2.22}$$

where we have used the fact that $h(x, y) = O(\epsilon)$. Similarly, we obtain

$$\widetilde{\mathbf{T}}\,\big|_{|\mathbf{x}|=\rho} = O(\epsilon/\rho^3) \quad \text{and} \quad \widetilde{\mathbf{T}}^m\,\big|_{|\mathbf{x}|=\rho} = O(\epsilon/\rho^3). \tag{2.23}$$

Since the area of Γ_ρ is proportional to ρ^2, combining (2.22) and (2.23) in the expression for I_3 yields (2.18).

Proof of Eq. 2.19. Recall that

$$I_4 = \int_{\Gamma_\rho} (\mathbf{u}^m - \mathbf{u}) \cdot \overline{\mathbf{T}}\mathbf{n} \, dS.$$

We note that $\overline{\mathbf{T}}\mathbf{n} = \mathbf{0}$ in the substrate. So, the only contribution to I_4 is when Γ_ρ coincides with the film. Furthermore, for $\rho \gg H$, the area of Γ_ρ coinciding with the film is proportional to ρH. Combining this with (2.22) yields (2.19).

Proof of Eq. 2.20. Recall that

$$I_5 = \frac{1}{2} \int_{\Gamma_\rho} \mathbf{u} \cdot (\widetilde{\mathbf{T}} - \widetilde{\mathbf{T}}_L^m)\mathbf{n} \, dS.$$

Let $\mathbf{v} = \mathbf{u} - \mathbf{u}_L^m$. Then, the integral can be rewritten as

$$\frac{1}{2}\int_{\Gamma_\rho} \mathbf{u}\cdot(\widehat{\mathbf{T}}\mathbf{v})\mathbf{n}\,dS, \tag{2.24}$$

where the operator $\widehat{\mathbf{T}}$ is defined through

$$(\widehat{T}v)_{ij} = \mu(\partial_i v_j + \partial_j v_i) + \lambda\delta_{ij}\partial_k v_k.$$

We now need to estimate $\widehat{\mathbf{T}}\mathbf{v}$. Let $\widetilde{h} = h - h^m$. We note that $\mathbf{v}$ satisfies the system

$$\begin{aligned}
\mu\Delta\mathbf{v} + (\lambda+\mu)\nabla(\nabla\cdot\mathbf{v}) &= \mathbf{0} \quad \text{for } z<0 \text{ and } |\mathbf{x}|<\rho,\\
(\widehat{\mathbf{T}}\mathbf{v})\mathbf{e}_3 &= -\sigma_1(\widetilde{h}_x(x,y)\mathbf{e}_1 + \widetilde{h}_y(x,y)\mathbf{e}_2)\\
&\quad \text{at } z=0 \text{ and } x^2+y^2<\rho^2,\\
\mathbf{v} &= \mathbf{0} \quad \text{for } z<0 \text{ and } |\mathbf{x}|=\rho.
\end{aligned} \tag{2.25}$$

Let $\mathbf{x} = \rho\mathbf{x}'$, $\mathbf{v}' = \mathbf{v}(\rho\mathbf{x}')$ and $\widetilde{h}'(x',y') = \widetilde{h}(\rho x', \rho y')$. Then, the system given by (2.25) can be transformed into the following system:

$$\begin{aligned}
\mu\Delta'\mathbf{v}' + (\lambda+\mu)\nabla'(\nabla'\cdot\mathbf{v}') &= \mathbf{0} \quad \text{for } z'<0 \text{ and } |\mathbf{x}'|<1,\\
(\widehat{\mathbf{T}}'\mathbf{v}')\mathbf{e}_3 &= -\sigma_1(\widetilde{h}'_{x'}(x',y')\mathbf{e}_1 + \widetilde{h}'_{y'}(x',y')\mathbf{e}_2)\\
&\quad \text{at } z'=0 \text{ and } x'^2+y'^2<1,\\
\mathbf{v}' &= \mathbf{0} \quad \text{for } z'<0 \text{ and } |\mathbf{x}'|=1.
\end{aligned} \tag{2.26}$$

For $\rho > R$, the solution to this problem can be written as

$$\mathbf{v}' = \sigma_1 \int\int_{s^2+t^2\le(R/\rho)^2} \mathbf{f}_1(x'-s, y'-t, z')\widetilde{h}'(s,t)\;dsdt,$$

where

$$\mathbf{f}_1 = \frac{\partial}{\partial x}\mathbf{G}_1\mathbf{e}_1 + \frac{\partial}{\partial y}\mathbf{G}_1\mathbf{e}_2,$$

$\mathbf{G}_1$ is the Green's tensor for (2.26), and we have used the fact that $\widetilde{h}$ is supported on the disc of radius R.

Since

$$\widehat{\mathbf{T}}\mathbf{v} = \rho^{-1}\,\widehat{\mathbf{T}}'\mathbf{v}',$$

we have

$$\widehat{\mathbf{T}}\mathbf{v} = \frac{\sigma_1}{\rho}\int\int_{s^2+t^2\le(R/\rho)^2} \widehat{\mathbf{T}}'\mathbf{f}_1(x'-s,y'-t,z)\widetilde{h}'(s,t)\,dsdt = O(\epsilon/\rho^3).$$

We note that $\widehat{\mathbf{T}}'\mathbf{f}_1(x'-s,y'-t,z) = O(1)$ and $\widetilde{h}'(s,t) = O(\epsilon)$. Hence, the integrand is $O(\epsilon)$. Combining this with (2.22) and (2.24) gives (2.20).

Proof of Eq. 2.21. Recall that

$$I_6 = \frac{1}{2}\int_{\Gamma^m}(\mathbf{u}_L^m - \mathbf{u}^m)\cdot\overline{\mathbf{T}}\mathbf{n}\,dS.$$

For $\rho > R$, we can use (2.15) and the leading order approximation of the normal to rewrite I_6 as

$$I_6 = \frac{\sigma_1}{2}\int\int_{x^2+y^2\le R^2}(\mathbf{u}_L^m(x,y,0)-\mathbf{u}^m(x,y,0))\cdot(h_x^m(x,y)\mathbf{e}_1+h_y^m(x,y)\mathbf{e}_2)\,dxdy. \quad (2.27)$$

Let $\mathbf{w} = \mathbf{u}_L^m - \mathbf{u}^m$ and $\widetilde{\mathbf{u}} = \mathbf{u} - \mathbf{u}^m$. We recall that $\mathbf{u}_L^m(|\mathbf{x}| = \rho) = \mathbf{u}(|\mathbf{x}| = \rho)$. Then, since $\mathbf{u}_L^m$ and $\mathbf{u}^m$ satisfy the first two equations of (2.16) on Ω_ρ, with h replaced by h^m, $\mathbf{w}$ satisfies the following system:

$$\begin{aligned}
\mu\Delta\mathbf{w} + (\lambda+\mu)\nabla(\nabla\cdot\mathbf{w}) &= \mathbf{0} \quad \text{for } z<0 \text{ and } |\mathbf{x}|<\rho,\\
(\widehat{\mathbf{T}}\mathbf{w})\mathbf{e}_3 &= \mathbf{0} \quad \text{at } z=0 \text{ and } |\mathbf{x}|\le\rho,\\
\mathbf{w} &= \widetilde{\mathbf{u}} \quad \text{at } z<0 \text{ and } |\mathbf{x}|=\rho. \qquad (2.28)
\end{aligned}$$

We note that $\widetilde{\mathbf{u}}$ satisfies (2.16) with h replaced by $\widetilde{h}$. Then, appealing to (2.17), we find

$$\widetilde{\mathbf{u}} = \sigma_1 \int\int_{x'^2+y'^2\le R^2} \mathbf{f}(x-x', y-y', z)\widetilde{h}(x', y')\ dx'dy'.$$

We need to evaluate $\widetilde{\mathbf{u}}$ on the lower hemisphere of radius ρ centered at $\mathbf{x} = (0,0,0)$. We begin by converting the above integral to polar coordinates:

$$\widetilde{\mathbf{u}} = \sigma_1 \int_0^{2\pi}\int_0^R \mathbf{f}(x - s\cos\beta, y - s\sin\beta, z)\widetilde{h}(s\cos\beta, s\sin\beta)s\ dsd\beta.$$

Let $(x,y,z) = \rho(\sin\varphi\cos\theta, \sin\varphi\sin\theta, \cos\varphi)$ and substitute this into the integral above. Then, writing the integrand as a Taylor series in s and expanding in terms of $1/\rho$, we have

$$\begin{aligned}
\widetilde{\mathbf{u}}\,\big|_{|\mathbf{x}|=\rho} &= \sigma_1 \sum_{n=0}^{\infty}\sum_{i=0}^{\lceil\frac{n+1}{2}\rceil-1}\sum_{j=0}^{n-2i} \frac{\binom{n-2i}{j}\int_0^{2\pi} a_n(\beta)(\cos\beta)^j(\sin\beta)^{n-2i-j}\ d\beta}{\rho^{n+2}}\mathbf{b}_{nij}(\varphi,\theta)\\
&+ \sigma_1 \sum_{n=1}^{\infty}\sum_{i=0}^{\lceil\frac{n}{2}\rceil-1}\sum_{j=0}^{n-1-2i} \frac{\binom{n-1-2i}{j}\int_0^{2\pi} a_n(\beta)(\cos\beta)^{j+1}(\sin\beta)^{n-1-2i-j}\ d\beta}{\rho^{n+2}}\mathbf{c}_{nij}(\varphi,\theta)\\
&+ \sigma_1 \sum_{n=1}^{\infty}\sum_{i=0}^{\lceil\frac{n}{2}\rceil-1}\sum_{j=0}^{n-1-2i} \frac{\binom{n-1-2i}{j}\int_0^{2\pi} a_n(\beta)(\cos\beta)^{j}(\sin\beta)^{n-2i-j}\ d\beta}{\rho^{n+2}}\mathbf{d}_{nij}(\varphi,\theta)
\end{aligned}$$

where $a_n(\beta) = \int_0^R \widetilde{h}(s\cos\beta, s\sin\beta)s^{n+1}\ ds$,

$$\mathbf{b}_{nij}(\varphi,\theta) = \frac{(-1)^{i+1}\prod_{k=0}^{2i-1}(n-k)}{4\pi n!\mu(\lambda+\mu)}\begin{bmatrix}
\frac{(\cos\theta)^{j+1}(\sin\theta)^{n-2i-j}(\sin\varphi)^{n+1-2i}}{2^i\cdot i!}\cdot\\
\Big((\lambda+\mu)(\cos\varphi)^2\prod_{k=0}^{n+1-i}(1+2k) - (\lambda+2\mu)\prod_{k=0}^{n-i}(1+2k)\Big)\\
\frac{(\cos\theta)^{j}(\sin\theta)^{n-2i-j+1}(\sin\varphi)^{n+1-2i}}{2^i\cdot i!}\cdot\\
\Big((\lambda+\mu)(\cos\varphi)^2\prod_{k=0}^{n+1-i}(1+2k) - (\lambda+2\mu)\prod_{k=0}^{n-i}(1+2k)\Big)\\
\frac{(\cos\theta)^{j}(\sin\theta)^{n-2i-j}(\sin\varphi)^{n-2i}\cos\varphi}{2^i\cdot i!}\cdot\\
\Big((\lambda+\mu)(\cos\varphi)^2\prod_{k=0}^{n+1-i}(1+2k) - \lambda\prod_{k=0}^{n-i}(1+2k)\Big)
\end{bmatrix}$$

for $n \in [0,\infty)$, $i \in [0, \lceil \frac{n+1}{2} \rceil - 1]$ and $j \in [0, n-2i]$,

$$\mathbf{c}_{nij}(\varphi,\theta) = \frac{(-1)^i \prod_{k=0}^{2i-1}(n-1-k)}{4\pi(n-1)!\mu(\lambda+\mu)} \begin{bmatrix} \frac{(\cos\theta)^j (\sin\theta)^{n-1-2i-j}(\sin\varphi)^{n-1-2i}}{2^i \cdot i!} \cdot \\ \left((\lambda+\mu)(\cos\varphi)^2 \prod_{k=0}^{n-i}(1+2k) - \lambda \prod_{k=0}^{n-1-i}(1+2k)\right) \\ 0 \\ 0 \end{bmatrix}$$

for $n \in [1,\infty)$, $i \in [0, \lceil \frac{n}{2} \rceil - 1]$ and $j \in [0, n-1-2i]$,

$$\mathbf{d}_{nij}(\varphi,\theta) = \frac{(-1)^i \prod_{k=0}^{2i-1}(n-1-k)}{4\pi(n-1)!\mu(\lambda+\mu)} \begin{bmatrix} 0 \\ \frac{(\cos\theta)^j (\sin\theta)^{n-1-2i-j}(\sin\varphi)^{n-1-2i}}{2^i \cdot i!} \cdot \\ \left((\lambda+\mu)(\cos\varphi)^2 \prod_{k=0}^{n-i}(1+2k) - \lambda \prod_{k=0}^{n-1-i}(1+2k)\right) \\ 0 \end{bmatrix}$$

for $n \in [1,\infty)$, $i \in [0, \lceil \frac{n}{2} \rceil - 1]$ and $j \in [0, n-1-2i]$.

Define

$$\begin{aligned} B_{nij} &= \binom{n-2i}{j} \int_0^{2\pi} a_n(\beta)(\cos\beta)^j (\sin\beta)^{n-2i-j}\, d\beta, \\ C_{nij} &= \binom{n-1-2i}{j} \int_0^{2\pi} a_n(\beta)(\cos\beta)^{j+1} (\sin\beta)^{n-1-2i-j}\, d\beta, \text{ and} \\ D_{nij} &= \binom{n-1-2i}{j} \int_0^{2\pi} a_n(\beta)(\cos\beta)^j (\sin\beta)^{n-2i-j}\, d\beta. \end{aligned}$$

We can now write the solution of (2.28) as

$$\begin{aligned} \mathbf{w} = \sigma_1 \sum_{n=0}^{\infty} \sum_{i=0}^{\lceil \frac{n+1}{2} \rceil - 1} \sum_{j=0}^{n-2i} \frac{B_{nij} \mathbf{w}_{nij}^1 \left(\frac{\mathbf{x}}{\rho}\right)}{\rho^{n+2}} \\ + \sigma_1 \sum_{n=1}^{\infty} \sum_{i=0}^{\lceil \frac{n}{2} \rceil - 1} \sum_{j=0}^{n-1-2i} \left(\frac{C_{nij} \mathbf{w}_{nij}^2 \left(\frac{\mathbf{x}}{\rho}\right) + D_{nij} \mathbf{w}_{nij}^3 \left(\frac{\mathbf{x}}{\rho}\right)}{\rho^{n+2}} \right), \end{aligned} \tag{2.29}$$

where $\mathbf{w}^k_{nij}$ satisfies (2.28) except that the subsurface boundary condition is replaced by

$$\mathbf{w}^k_{nij} = \begin{cases} \mathbf{b}_{nij} & \text{if } k = 1 \\ \mathbf{c}_{nij} & \text{if } k = 2 \\ \mathbf{d}_{nij} & \text{if } k = 3 \end{cases} \qquad \text{for} \quad |\mathbf{x}| = \rho \text{ and } z < 0. \tag{2.30}$$

We note that the only term in (2.29) corresponding to $1/\rho^2$ in the expansion of the solution is $B_{000}\mathbf{w}^1_{000}(\mathbf{x}/\rho)$. We recall from (2.27) that

$$I_6 = \frac{\sigma_1}{2} \int\int_{x^2+y^2 \le R^2} \mathbf{w}(x, y, 0) \cdot (h^m_x(x, y)\mathbf{e}_1 + h^m_y(x, y)\mathbf{e}_2)\, dxdy.$$

Since $\mathbf{w}^1_{000}(x, y, z)$ is a solution to (2.28) with the boundary condition replaced by (2.30), so too is $\widetilde{\mathbf{w}}^1_{000}(x, y, z)$ where

$$\widetilde{\mathbf{w}}^1_{000}(x, y, z) = \begin{bmatrix} -{}^1\mathbf{w}^1_{000}(-x, -y, z) \\ -{}^2\mathbf{w}^1_{000}(-x, -y, z) \\ {}^3\mathbf{w}^1_{000}(-x, -y, z) \end{bmatrix}$$

and ${}^l\mathbf{w}^1_{000}$ denotes the l-th component of $\mathbf{w}^1_{000}$. Provided the solution is unique, it follows that ${}^1\mathbf{w}^1_{000}(0, 0, 0) = 0$ and ${}^2\mathbf{w}^1_{000}(0, 0, 0) = 0$. Therefore, $\mathbf{e}_1 \cdot \mathbf{w}^1_{000}(0, 0, 0) = 0$ and $\mathbf{e}_2 \cdot \mathbf{w}^1_{000}(0, 0, 0) = 0$. It then follows from (2.29) that

$$\mathbf{e}_1 \cdot \mathbf{w}(0, 0, 0) = O(1/\rho^3)$$

and

$$\mathbf{e}_2 \cdot \mathbf{w}(0, 0, 0) = O(1/\rho^3).$$

Furthermore, differentiating (2.29), we find that

$$\partial_x((\mathbf{e}_1 + \mathbf{e}_2) \cdot \mathbf{w})(0, 0, 0) = O(1/\rho^3)$$

and

$$\partial_y((\mathbf{e}_1 + \mathbf{e}_2) \cdot \mathbf{w})(0,0,0) = O(1/\rho^3).$$

Therefore, we conclude that

$$(\mathbf{e}_1 + \mathbf{e}_2) \cdot \mathbf{w}(x,y,0) = O(1/\rho^3) \quad \text{provided} \quad x^2 + y^2 = O(1).$$

Substituting this last result into (2.27) and using the fact that both $h_x = O(\epsilon)$ and $h_y = O(\epsilon)$, we obtain (2.21).

2.3 Summary

A common issue one must deal with in the simulation of heteroepitaxial growth using KMC is the long-range nature of the elastic interactions. Schulze and Smereka previously considered a local approximation technique that was observed to yield highly accurate approximations of the energy barrier for adatom diffusion in numerical computations on a two-dimensional lattice. Using a continuum analogue of the discrete model, they were able to explain these results and derive estimates for the error as a function of the size of the local region.

In this current work, we have extended those previous results to a three-dimensional lattice. As one may expect, we have shown that the error scales by a factor of one over the size of the box in the localized approximation when transitioning from a two-dimensional to a three-dimensional lattice. By comparing this result to a more intuitive Energy Truncation Approximation, we have further demonstrated the high accuracy of the Energy Localization Approximation and its utility in KMC simulations of heteroepitaxial growth.

Chapter 3

Grain Boundary Migration Driven By Curvature

3.1 Introduction

A perfect crystal is one in which the atoms of a crystalline material follow an ordered packing determined by unit cell parameters (see Figure 3.3 for a FCC crystal). The regular patterns within most crystalline materials, however, are interrupted by crystallographic defects. One such planar defect is a grain boundary, which is the

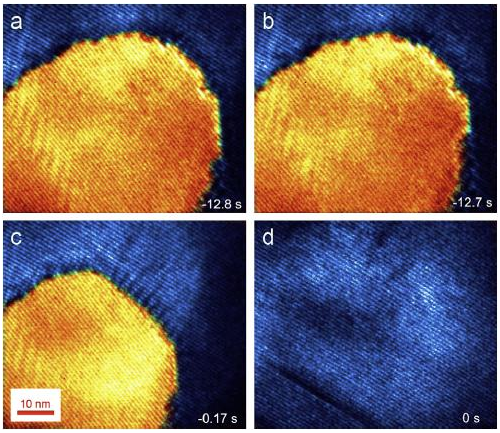

Figure 3.1: High resolution electron microscopy (HREM) observation of Au island grain shrinkage atop a Ge substrate [19].

interface between two grains, or oriented crystals, in a polycrystalline material. Crystal defects within a metal affect many properties of the metal. Grain size has been shown to affect the strength of metals, known as the Hall-Petch relation ([9], [18]), as well as the electrical and thermal conductivity [16]. Since grain size is largely controlled by grain boundary migration, there is considerable interest in understanding the mechanisms of grain boundary migration in order to optimize processes such as the annealing and forging of metals [31].

In the absence of external driving forces, grain boundary migration is driven by the curvature of the grain boundaries (see Figure 3.1). The motion of grain boundaries under the effect of curvature can be modeled by the relation

$$v_n = -\frac{dR}{dt} \propto \kappa,$$

where v_n is the normal growth velocity of the boundary, R is the radius of the grain, and κ is the local curvature of the grain ([4],[10]). Then, in the case of a spherical grain, one has the parabolic growth law

$$R^2(t) = R_0^2 - Mt, \tag{3.1}$$

where M is a mobility constant that may depend on the misorientation at a grain boundary ([2], [4]). Experiments, however, show that the predicted $n = 2$ growth law is a lower bound and the actual observed value lies somewhere between $n = 2$ and $n = 4$ for many metals ([1], [7]).

One of the more commonly used discrete models for grain boundary migration is the Potts model. In the Potts model, a regular lattice is subdivided into regions by numerating the lattice with spins corresponding to orientations (see Figure 3.2). The q-state Potts model is a generalization of the Ising model (corresponding to $q = 2$), which is where the term spin originates as it was originally used to study phase transitions in magnetic materials. The Hamiltonian of the given system is based on

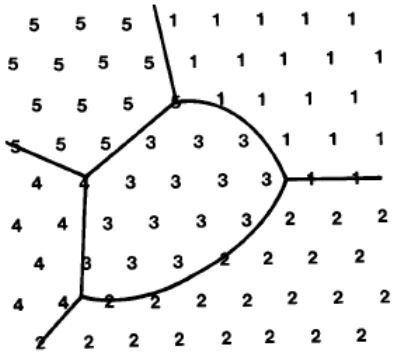

Figure 3.2: Sample microstructure on a triangular lattice showing the boundaries of five grains represented by spin numbers [26].

interaction pairs and is given by

$$H = \frac{1}{2} \sum_{(i,j)} J_{q_i,q_j},$$

where q_k is the state of the grain at site k and J_{q_i,q_j} is the interaction energy between sites i and j. To simplify the model, typically only nearest neighbors and possibly next-nearest neighbors are considered in the Hamiltonian. In simulations regarding grain growth of an isotropic material, a typical choice for the interaction energy is $J_{q_i,q_j} = J(1-\delta_{q_i,q_j})$ ([1], [28]). Then, only interfacial energies between unlike neighbors contribute to the total energy of the system and the Hamiltonian simplifies to

$$H = \frac{J}{2} \sum_{(i,j)} (1 - \delta_{q_i,q_j}).$$

This Hamiltonian measures the excess free energy of the system and is reduced as the system moves towards a perfect crystal. Using the Hamiltonian, grain growth is simulated using a Monte Carlo method in which steps are accepted based on Boltzmann statistics.

Whereas the Potts model is a coarse-grained model, we propose an atomistic KMC model for the case of arbitrarily oriented FCC crystals. The lattice of a FCC crystal is easily constructed from the repetition of the FCC unit cell, which is a cube with

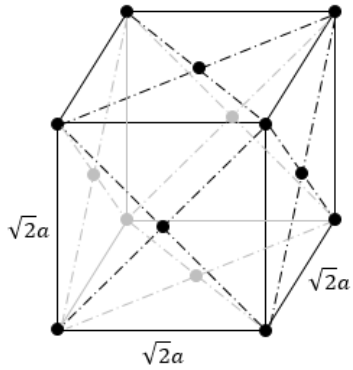

Figure 3.3: Unit cell of a FCC crystal, where a is the lattice spacing and dotted lines denote nearest neighbors on the faces. Each atom has 12 nearest neighbors and 6 next-nearest neighbors.

atoms at each of the corners as well as the center of each of the faces (see Figure 3.3). Based on the result given by (3.1), we will track the surface area of a spherical grain embedded inside a second grain as it shrinks. In order to do this, we will need to estimate the radius of the embedded grain at each time step. One way to do this is to consider how many atoms lie in a unit cell. We first normalize the lattice by setting $a = \sqrt{2}$ so that next-nearest neighbors are two units apart and each of the lattice locations correspond to integer triples in an array. Then, the volume of the unit cell is eight cubic units. We notice that each of the eight corner atoms contribute one-eighth of an atom to the unit cell. Likewise, each of the six atoms on the faces contribute one-half of an atom. Since the unit cell contains four atoms and has a volume of eight cubic units, we find that there is half an atom per cubic unit. Knowing this, we can count the number of atoms in the grain and multiply by two to get the volume of the grain. Then, we use the volume of a sphere to estimate the radius.

In Section 3.2, we propose the model and discuss how it is similar to, and differs from, a typical bond-counting KMC model. In Section 3.3, we discuss some of the limitations of our model. In Section 3.4, we discuss how the model is implemented in C++. In Section 3.5, we give some results and make comparisons to MD simulations. Finally, we sum up the results in Section 3.6 and provide evidence as to why we expect the model to be able to capture the parabolic law given by (3.1).

3.2 KMC Model

The model proposed here maintains a close analogy with standard bond-counting KMC models for single grain surface diffusion. As with any KMC model, the state-space must first be defined (Section 3.2.1). Then, rules must be implemented for how atoms are allowed to hop from one site to another (Section 3.2.2). Lastly, the rates at which these transitions occur must be provided (Section 3.2.3).

3.2.1 State-space

As previously mentioned, our model is able to simulate the evolution of arbitrarily oriented FCC crystals. In order to test the theoretical parabolic growth law given by (3.1), we will consider the case of a spherical grain embedded inside a second grain. To this end, we have developed a KMC model that works with the two lattices simultaneously. While the embedded grain must completely lie inside the second grain, it is allowed to undergo a coordinate transformation via an arbitrary rotation and displacement. For each of the two FCC orientations, we define the lattices as all integer-valued linear combinations of three basis vectors

$$\mathbf{x}_{ijk} = i\mathbf{a} + j\mathbf{b} + k\mathbf{c},$$

where $\mathbf{a} = \frac{a}{\sqrt{2}}\mathbf{i} + \frac{a}{\sqrt{2}}\mathbf{j}$, $\mathbf{b} = \frac{a}{\sqrt{2}}\mathbf{i} - \frac{a}{\sqrt{2}}\mathbf{j}$, $\mathbf{c} = \frac{a}{\sqrt{2}}\mathbf{j} + \frac{a}{\sqrt{2}}\mathbf{k}$, and a is the lattice spacing. Furthermore, we define an occupation array I^{α}_{ijk} for each of the two lattices $\alpha \in \{1, 2\}$ that indicates whether or not an atom is present at a given site (i, j, k) of a lattice. It is typical to use 0's to denote an unoccupied site and 1's to denote an occupied site. At each step, the possible configurations that the current state may transition to must be known. For this, we create a list of rules for what moves are allowed.

3.2.2 Allowed Transitions

While it is clear that an already occupied site cannot be occupied by a second atom, we further define a "forbidden zone" to ensure the physically reasonable assumption that no two atoms on any grain come too close to one another. That is, a lattice site will be considered unoccupiable, i.e. in a "forbidden zone" that cannot be hopped into, if any of its neighbors within a given distance ($d_{xx'} < d_f$) on another lattice are currently occupied. Here, $d_{xx'}$ is the distance between the site x and any occupied site x' on another lattice, d_f is the specified forbidden zone. Allowed transitions in our multi-grain model satisfy all of the following:

1. Fully coordinated atoms with respect to an atom's own lattice are not allowed to move. By fully coordinated we mean that all 12 of its nearest neighbor sites are occupied.

2. Only single atom moves to unoccupied sites are allowed.

3. Moves are either to nearest neighbor sites on the atom's current lattice or to sites within an "admissible zone" ($d_{xx'} < d_a$) on another lattice that have an occupied neighbor. Here, d_a is the specified admissible zone. Furthermore, requiring the site to have an occupied neighbor ensures that the site is connected to another grain. This rule ensures the physically reasonable assumption that atoms can hop from one grain to another as long as the target site is within a reasonable distance.

4. The destination site cannot be in the forbidden zone defined above, i.e. even though a destination on the current lattice may be unoccupied, it may be too close to an occupied site on another lattice.

These rules are rather restrictive and leave room only for a relatively small number of allowed transitions in the vicinity of grain boundaries. For motion of grain boundaries to be possible upon initialization, we further introduce a sufficiently large

gap (vacancies) between grain boundaries. As the system evolves, these vacancies either become frozen or migrate to the center of the embedded grain.

3.2.3 Transitional Rates

To complete the model, we have to assume rates for the allowed transitions defined in the previous section. This is done in a way that is analogous to the simplest bond-counting KMC models. In the case of two grains, the rates depend exponentially on the number of occupied nearest neighbor sites on an atom's own lattice, N^{α}, and the number of occupied nearest neighbor sites on the second lattice, N^{β}. An occupied site on the second lattice is considered a nearest neighbor if it is no more than a bond length away. This exponential factor is then multiplied by the number of accessible sites on both lattices, $M^{\alpha\beta}$. We note here that diffusive moves along a boundary and transitional moves across the boundary are not distinguished. That is, each move is equally probabilistic. Then, the hopping rate associated with an atom is given by

$$r = kM^{\alpha\beta}e^{-N^{\alpha}\cdot E^{\alpha}-N^{\beta}\cdot E^{\beta}}, \tag{3.2}$$

where E^{α}, E^{β} are bond-strength parameters and k is a parameter that determines the overall timescale for hops to take place. In the case of a homogeneous material, we set $E^{\alpha} = E^{\beta}$. It is clear from (3.2) that atoms tend to move to increase their coordination, which is consistent with the fact that atoms naturally move to a more stable state. As a result, atoms tend to move from convex surfaces to concave surfaces and the grain growth kinetics are driven by curvature.

3.3 Limitations

Since we are considering an atomistic model with a structured lattice, there are several defect features that we will not be able to capture that can be recreated in other models such as MD and phase-field models. One such imperfection in a crystal is

the creation and distribution of dislocations, which are line defects where the crystal structure is broken. Since each lattice is fixed in our model, it is not possible to break the crystal structure and form a dislocation. An important consideration as a result of the formation of dislocations in a crystal is elastic deformations. Furthermore, the fixed lattice structure does not allow for the irregular packing of atoms near grain boundaries, which also is a cause for elastic deformations. Unlike our treatment of heteroepitaxial thin films (see Chapter 2), transitional rates in the current model do not take into account elastic effects. While it is accepted that grain boundary migration leads to a reduction in the overall energy of a polycrystalline system, there is both theoretical [4] and numerical [29] evidence that the overall energy of the system can be reduced via grain rotation as well. Since our model only allows for single atom moves from one fixed lattice to another, it is impossible for our model to replicate these results.

3.4 Implementation

As previously mentioned, the code implementing the KMC algorithm given in Section 3.2 was written in C++. Furthermore, we currently consider the case of a spherical grain embedded inside a second grain. In order to create the occupation arrays I^{α}_{ijk}, each grain is stored in a cubic lattice by checkering the lattice via parity:

$$L^{\alpha} \equiv \{(i,j,k) \in I^{\alpha}_{ijk} \mid (i+j+k) \bmod 2 = (i'+j'+k') \bmod 2\},$$

where L^{α} is the FCC lattice of grain $\alpha \in \{1,2\}$ and (i',j',k') is the center of the lattice. We hold the inner grain fixed and rotate the outer grain with respect to each of the principal axes. We first rotate about the x-axis, then the y-axis, and finally the z-axis. An alternative would be to declare a rotational axis first and then rotate about it. Along with arbitrary rotations, we allow the grains to be translated so that they do not necessarily coincide.

To initialize the grains, we first sweep through each lattice searching for sites that are within the radius of the outer grain and lie on the checkerboard previously created. Any site that is within the radius of the outer grain and has the same parity as the central site is set to -1. All other sites are set to -2 and are unaccessible at all times. We further note here that we have chosen to use a free surface at the boundary of the outer grain. Next, we search through the lattice of the inner grain looking for sites that are within the radius of the inner grain. Rather than following the typical numbering of setting occupied sites to 1 and unoccupied sites to 0, we number the occupied sites starting with 0 and leave all unoccupied sites as -1 meaning that they are accessible as long as a transition to this site does not violate any of the rules in Section 3.2.2. Then, we search through the lattice of the outer grain looking for sites that are within the radius of the outer grain, outside the radius of the inner grain plus the gap, and aren't within the forbidden zone. These sites are numbered, continuing on from the sites numbered in the inner grain. One reason for numbering the sites this way is that we will be storing certain information about each of the atoms, which we can easily look up by number.

Once the occupied sites are numbered, the lattice coordinates (i, j, k) of the atoms are stored. Furthermore, we record which grain the atom is in (0 for inner grain and 1 for outer grain). Next, we count the number of nearest neighbors of each atom in their own grain and store this number. Furthermore, we count the number of nearest neighbors of each atom in the second grain and store this number. Along with these counts, we create an inverse list that lists each atom according to the number of nearest neighbors that it has on each lattice. The row number in this list is stored for each atom. This list is particularly useful when choosing an atom to hop. We then count the number of accessible sites to each atom on both lattices according to the rules in Section 3.2.2 and store this number.

To evolve the system, we first create a list of partial sums, S_i with $0 \leq i \leq 156$, that is calculated by multiplying the hopping rate corresponding to an atom with m nearest neighbors on its own lattice and n nearest neighbors on the second lattice

by the total number of accessible moves for atoms with those neighbor counts. This quantity is added to the previous sum S_{i-1} to obtain S_i, where $S_0 \equiv 0$. We note that $i = 13m + n + 1$, where $0 \leq m \leq 11$ and $0 \leq n \leq 12$. By design, atoms that are fully occupied with respect to its own lattice cannot hop. So, the list of partial sums is a vector of length 157.

Next, we choose a uniformly distributed random number, u, on $[0, 1)$ and find the first i such that $uS_{156} < S_i$. We then choose the corresponding atom in column $i - 1$ of the inverse list whose row is the first row corresponding to $k = 0$ if

$$M_{\#0} \geq \frac{uS_{156} - S_{i-1}}{\widetilde{r}_{i-1}},$$

or the $(k + 1)$-st row corresponding to $k \geq 1$ such that

$$\sum_{j=0}^{k-1} M_{\#j} < \frac{uS_{156} - S_{i-1}}{\widetilde{r}_{i-1}} \leq \sum_{j=0}^{k} M_{\#j},$$

where $M_{\#j}$ denotes the number of accessible sites to the atom in row j of column $i - 1$ and $\widetilde{r}_{i-1}$ denotes the hopping rate for an atom with m nearest neighbors on its own lattice and n nearest neighbors on the second lattice such that $i - 1 = 13m + n$.

The transition that the selected atom makes is chosen analogously. We find the first $l > 0$ such that

$$l \geq \frac{uS_{156} - S_{i-1}}{\widetilde{r}_{i-1}}$$

if $k = 0$, or

$$l \geq \frac{uS_{156} - S_{i-1}}{\widetilde{r}_{i-1}} - \sum_{j=0}^{k-1} M_{\#j}.$$

if $k \geq 1$. Since $0 < l \leq M_{\#k}$, we cycle through the available transitions for the selected atom, $\#k$, and choose the l-th possible transition.

Once an atom and transition are selected, we do a search for which atoms need an updated count of accessible sites and nearest neighbors on the second lattice. This is done by searching a cubic volume around the atom's old location that extends a

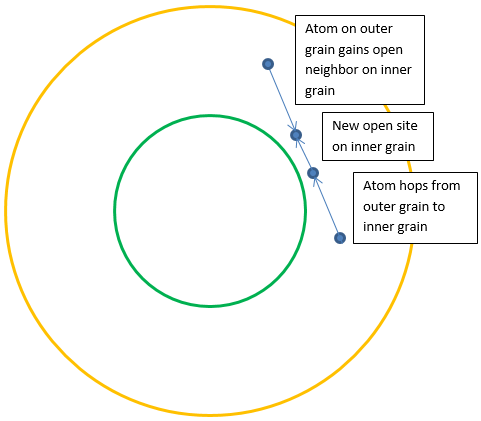

Figure 3.4: Upper-bound on search radius for localized change in nearest neighbor and accessible site counts once a transition has taken place.

distance of $2d_a + a$ in any of the principal directions, where we are using $a = \sqrt{2}$ and $d_a = s \cdot a$ for some scalar $s > 0$. Both lattices are swept inside this volume and all atoms that are contained within it are stored in a list. This distance of $2d_a + a$ is an upper-bound that is observed in simulations (see Figure 3.4). We then update information on all the atoms that lost a neighbor on its own lattice as a result of the hop. After that, we update information about the atom that hopped and then information about all the atoms on the new lattice that gained a neighbor. Finally, we fully redo the search for accessible sites and nearest neighbors on the second lattice for each atom that was placed in the list above.

We note that this last update is not optimal and is rather inefficient. In fact, the majority of the CPU time is consumed here. We have found that >90% of the CPU time is just from this repeated search over the evolution of the system. For the choice of $d_a = a$, this means possibly updating information for ∼300 atoms, although there are only sparse changes. This is in contrast to a standard KMC model for single grain surface diffusion in which at most 24 sites require updates.

3.5 Results

We now present some simulations showing quantitative and qualitative agreement with theoretical predictions (see (3.1)), MD simulations, and experimental observations. For each simulation, the following parameters must be specified: radius of the inner grain (R_0), rotation about the x-axis (θ_x), rotation about the y-axis (θ_y), rotation about the z-axis (θ_z), gap size (d_g), forbidden zone (d_f), admissible zone (d_a), intra-grain bond strength (γ_1), inter-grain bond strength (γ_2), and the displacement of the center of the inner grain relative to the center of the outer grain (D). In the case of a homogeneous material, we assume that the intra-grain bond strength and inter-grain bond strength are equivalent.

For the results that follow, we hold the following parameters fixed unless stated otherwise: $R_0 = 12$, $\theta_x = \pi/6$, $\theta_y = \pi/9$, $\theta_z = 11\pi/18$, $D = \langle 0, 0, 0 \rangle$, $\gamma_1 = 5123/615$, and $\gamma_2 = 5123/615$. We note that the bond strengths have been chosen to be consistent with gold [8]. This leaves us with the parameters d_g, d_f, and d_a. Since our model only allows nearest neighbor moves on an atom's own lattice, we restrict $\sqrt{2} < d_a < 2$, where the upper-bound is the distance between next-nearest neighbors. If one considers the Lennard-Jones potential to model the interaction between a pair of atoms, the overall energy of the system is increased as the spacing between atoms decreases. For this reason, we keep the forbidden zone d_f close to, but slightly less than, a bond length. Also, the gap size d_g is kept close to the forbidden zone. If the gap size is too small, either no moves are possible or the action is driven by local hot spots where relatively few moves are allowed.

3.5.1 Parabolic Law

We first show that with suitable choices of parameters, the theoretical parabolic law can be recovered. We recall that the bond length is scaled such that $a = \sqrt{2}$, and we set $d_g = d_f = \frac{9}{10}\sqrt{2}$, $d_a = \frac{7}{5}\sqrt{2}$. Furthermore, we set $\gamma_2 = 0$. That is, the grains do not feel each other. As we see in Figure 3.5, the surface area of the grain decreases

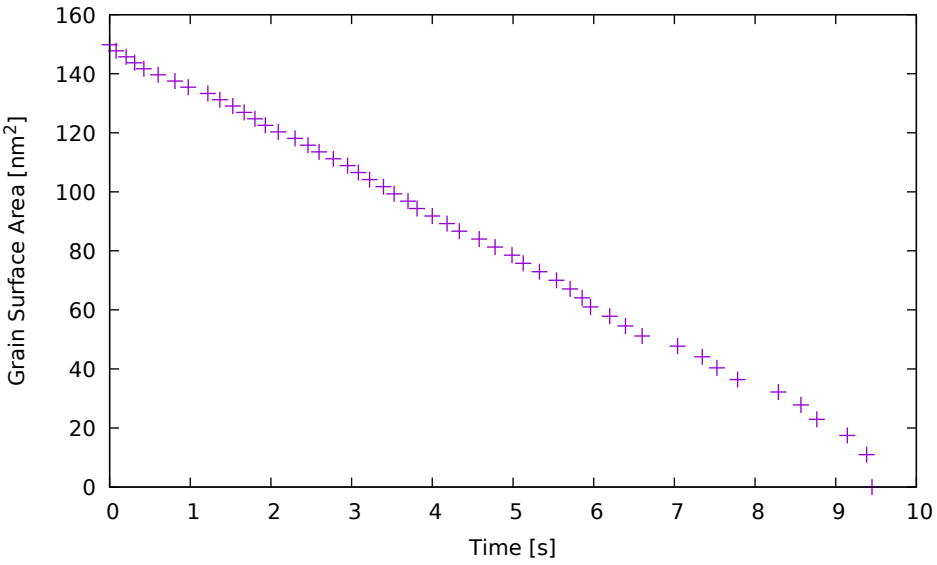

Figure 3.5: Plot of surface area vs. time showing parabolic growth law.

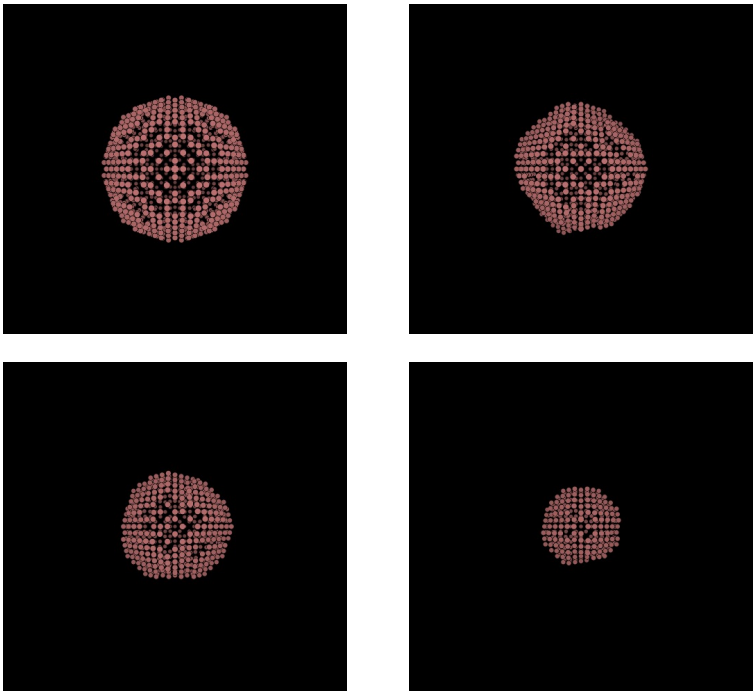

Figure 3.6: Snapshots of grain evolution showing that the grain maintains a spherical shape and facets during shrinkage. Snapshots were created using the Visual Molecular Dynamics (VMD) program. Only surface atoms are displayed.

linearly with time up until it nearly disappears. Furthermore, we see in Figure 3.6 that the grain maintains its shape and facets as it shrinks, which is in qualitative agreement with Radetic at al. [19]. From an atomistic viewpoint, planar regions are energetically preferred and steps are expected, as the most likely places for atoms to leave a grain are at the boundaries of incomplete planes [15]. As we see in the next section, the parabolic growth law breaks down once the inter-grain bond strength is turned on.

3.5.2 Non-parabolic Behavior

Radetic et al. [19] showed that in experiments of shrinking island grains in thin films of gold, there are long periods of inactivity followed by rapid periods of parabolic behavior correlated with the sudden motion of steps along facets or the elimination of entire facets. Implementing a MD simulation, they were able to reproduce these lab results for cylindrical grains (see Figure 3.7). We find similar results for suitable parameters. By turning the inter-grain bond strength on and keeping the remaining parameters the same as in Section 3.5.1, we see in Figure 3.8 that the parabolic growth law starts to break down. Furthermore, we see in Figure 3.9 that the behavior breaks down even more as we decrease the gap size to $d_g = \frac{4}{5}\sqrt{2}$. Namely, we start to see

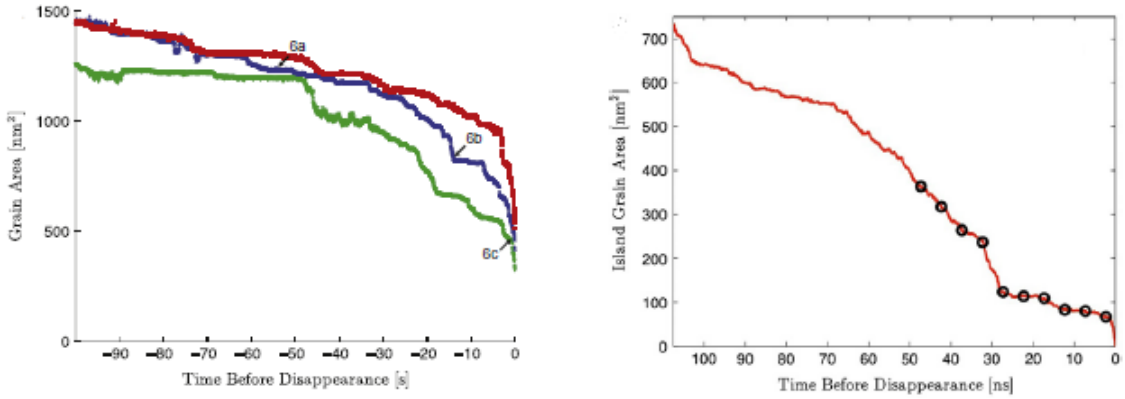

Figure 3.7: Experimental (left) and MD (right) plots of surface area vs. time for cylindrical Au grains showing non-parabolic growth.

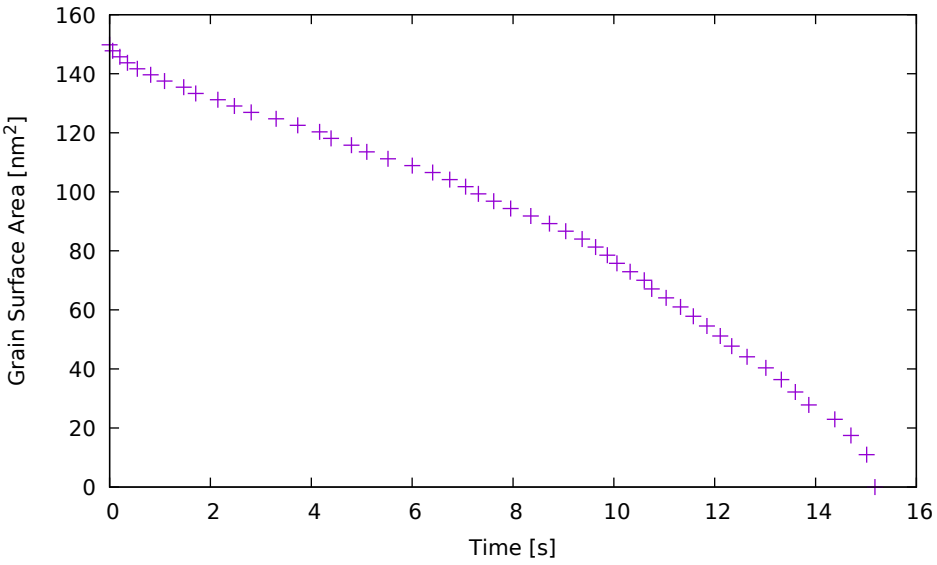

Figure 3.8: Plot of surface area vs. time showing how the parabolic growth law begins to break down.

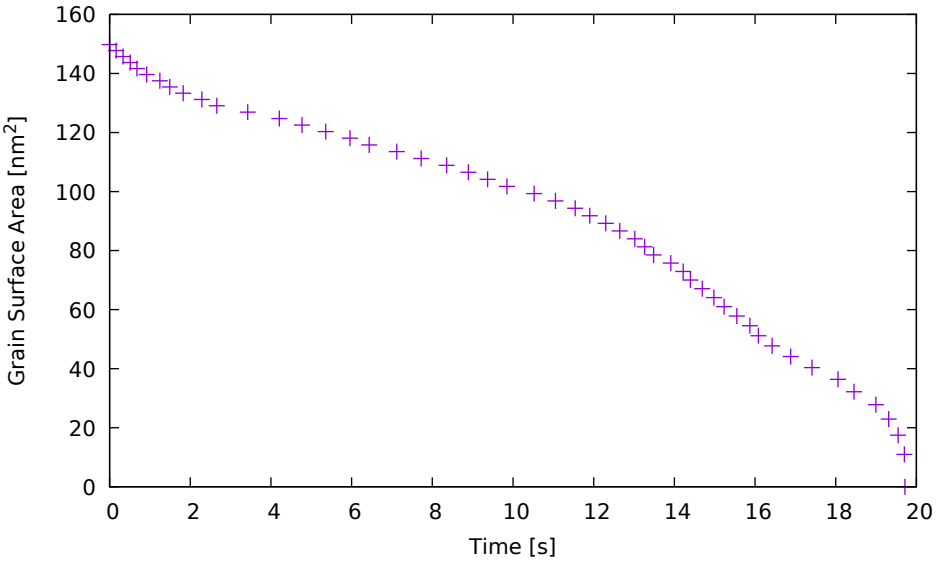

Figure 3.9: Plot of surface area vs. time showing non-parabolic growth.

periods of little to no activity followed by rapid movements as in Figure 3.7. These faster events correspond to the movement of facets, which is consistent with the observations of Radetic et al. [19].

3.6 Summary

As we have seen, both parabolic and non-parabolic behavior can be captured with our model for suitable choices of the parameters of the model. As we discuss in Chapter 4, we are interested in the relationship between the gap size, forbidden zone, and admissible zone. Specifically, we would like to know whether or not we can predict the behavior of shrinkage rates based on the choice of these parameters.

Here, we offer an explanation as to why we might expect to reproduce the parabolic law with the choice of parameters in Section 3.5.1. We note that the shrinkage of a grain, and therefore the motion of the grain boundary, is a result of inter-grain moves in which an atom hops from one grain lattice to the other. So, we ignore diffusive moves for the moment and focus solely on the available moves in an initial configuration for which an atom hops from one lattice to the other. Specifically, we track the total number of possible moves from the inner grain to the outer grain minus the total number of possible moves from the outer grain to the inner grain.

In Figure 3.10, we consider the difference in inter-grain moves for atoms with six nearest neighbors on its own lattice. Since the results of Section 3.5.1 are dependent on the inter-grain bond strength being set to zero, inter-grain neighbors are a non-factor and we only consider neighbors on an atom's own lattice. As we see, the dependence of inter-grain moves on radius is roughly linear, and this is consistent among all 12 possible coordinations. We note that the radius here corresponds to normalized distances in which $a = \sqrt{2}$. Furthermore, we ignore fully coordinated atoms, that is atoms with 12 nearest neighbors on its own lattice, since they are not allowed to move according to the rules established in Section 3.2.2.

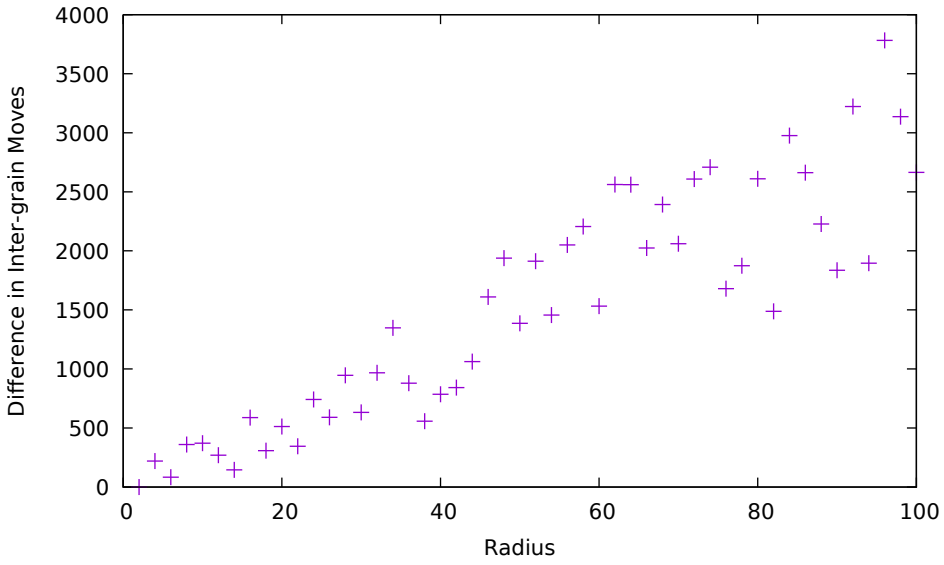

Figure 3.10: Plot of the difference in inter-grain moves vs. radius for atoms with 6 nearest neighbors on its own lattice.

We recall that in order to select a move, we select a uniformly distributed random number on $[0, S_{12})$, where S_{12} is the total rate of all possible transitions from the current configuration to another state. We note that the sum here runs to 12, as opposed to 156 from before, since there are only 12 possible coordinations for which moves are allowed. Furthermore, we note that for the overall process of atoms hopping from the inner grain to the outer grain,

$$S_{12} = \sum_{j=0}^{11} \widetilde{r}_j \cdot \widetilde{M}_j,$$

where $\widetilde{r}_j$ is the hopping rate for a single available move of an atom with j nearest neighbors on its own lattice and $\widetilde{M}_j$ is the difference in the total number of inter-grain moves from the inner grain to the outer grain available to atoms with j nearest neighbors on its own lattice. Since the rates $\widetilde{r}_j$ are constant and $\widetilde{M}_j \sim R$, we see that $S_{12} \sim R$.

Let's consider the ratio $\Delta R/\Delta t$ for each inter-grain move from the inner grain to the outer grain. Since $\Delta t = 1/S_{12}$ for each move, we have that $1/\Delta t \sim R$. We now

consider ΔR. We know that

$$R = \sqrt[3]{\frac{3V}{4\pi}}$$

for a sphere. Then,

$$\Delta R = \sqrt[3]{\frac{3V_f}{4\pi}} - \sqrt[3]{\frac{3V_i}{4\pi}}, \tag{3.3}$$

where V_i is the initial volume and V_f is the final volume of the inner grain after one atom has hopped from the lattice of the inner grain to the outer grain. As previously mentioned, there is half an atom per unit volume. Then, $V = 2N_A$, where N_A is the number of atoms on the inner grain. It follows from (3.3) that

$$\Delta R = \sqrt[3]{\frac{3}{2\pi}} \left(\sqrt[3]{N_A - 1} - \sqrt[3]{N_A} \right).$$

Furthermore, $\sqrt[3]{N_A - 1} \sim \sqrt[3]{N_A} - N_A^{-2/3}/3$. Then, to leading order,

$$\Delta R \sim -N_A^{-2/3} \sim -V_i^{-2/3} \sim -R^{-2}.$$

Therefore,

$$\frac{\Delta R}{\Delta t} \sim -\frac{R}{R^2} = -\frac{1}{R}.$$

That is, we recover the same scaling as the curvature of the grain.

Chapter 4

Summary and Future Directions

We have considered two applications of KMC algorithms to simulations of crystal growth and evolution in this dissertation. First, we provided an analysis of an Energy Localization Approximation applied to three-dimensional KMC simulations of heteroepitaxial growth (Chapter 2). We were able to further emphasize the results of Schulze and Smereka [22] by showing that while the error scales by a factor of one over the distance in the localized approximation of heteroepitaxial thin film growth for the case of an isolated island sitting on an unbounded and otherwise flat film on a flat substrate, a more intuitive Energy Truncation Approximation does not. Second, we proposed a KMC model for grain boundary migration driven by curvature for arbitrarily oriented FCC grains (Chapter 3). We compared simulation results with theoretical results and MD simulations, showing that our simulations compare favorably for suitable choices of parameters.

While we were able to show that our KMC model for grain boundary migration demonstrates growth kinetics observed in experiments and MD simulations, as well as predicted theoretically, there is still work to be done. First and foremost, we would like to better understand under what conditions the parabolic behavior breaks down. That is, can we predict the growth kinetics based on our choices of parameters? If so, are there physically reasonable parameters for which the parabolic law breaks

down? It would also be of interest to see if there is a relationship between the growth kinetics and misorientation as mentioned by Cahn and Taylor [4] and observed by Aust and Rutter [2]. As we mentioned at the end of Section 3.4, our local search for updates of accessible sites and nearest neighbor counts is inefficient and rather costly. Since these updates are non-sequential, one could speed up the search via parallelization. Otherwise, further investigation might be able to reduce the search radius by considering the relationship between the gap size, admissible zone, and forbidden zone as these are the three crucial parameters for determining allowed transitions.

Bibliography

[1] M. P. Anderson, D. J. Srolovitz, G. S. Grest, and P. S. Sahni. Computer simulation of grain growth–i. kinetics. *Acta Metall.*, 32:783–791, 1984. 28, 29

[2] K. T. Aust and J. W. Rutter. *Recovery and Recrystallization of Metals*. T.M.S.-A.I.M.E., New York, NY, 1962. 28, 46

[3] J. E. Ayers. *Heteroepitaxy of Semiconductors: Theory, Growth, and Characterization*. CRC Press, Boca Raton, FL, 2007. 5

[4] J. W. Cahn and J. E. Taylor. A unified approach to motion of grain boundaries, relative tangential translation along grain boundaries, and grain rotation. *Acta Mater.*, 52:4887–4898, 2004. 28, 34, 46

[5] P. Fratzl, J. L. Lebowitz, and O. Penrose. Modeling of phase separation in alloys with coherent elastic misfit. *J. Stat. Phys.*, 95:1429–1503, 1999. 8

[6] P. L. Gould. *Introduction to Linear Elasticity*. Springer-Verlag, New York, NY, 2 edition, 1994. 9

[7] F. Haessner and S. Hofmann. *Recrystallization of Metallic Materials*. Stuttgart, Germany, 1978. Edited by Dr. Riederer Verlag, pp 63-95. 28

[8] T. Halicioğlu and G. M. Pound. Calculation of potential energy parameters from crystalline state properties. *Phys. Status Solidi A*, 30:619–623, 1975. 38

[9] E. O. Hall. The deformation and ageing of mild steel: Iii discussion and results. *Proc. Phys. Soc. London, Sec. B*, 64:747–753, 1951. 28

[10] M. Hillert. On the theory of normal and abnormal grain growth. *Acta Metall.*, 13:227–238, 1965. 28

[11] F. Jonsdottir and L. B. Freund. Equilibrium surface roughness of a strained epitaxial film due to surface diffusion induced by interface misfit dislocations. *Mech. Mater.*, 20:337–349, 1995. 5

[12] C. H. Lam, C. K. Lee, and L. M. Sander. Competing roughening mechanisms in strained heteroepitaxy: A fast kinetic monte carlo study. *Phys. Rev. Lett.*, 89:216102(1–4), 2002. 5, 6, 11

[13] L. D. Landau and E. M. Lifshitz. *Theory of Elasticity*. Pergamon Press, Oxford, England, 3 edition, 1986. 18, 53

[14] M. T. Lung, C. H. Lam, and L. M. Sander. Island, pit, and groove formation in strained heteroepitaxy. *Phys. Rev. Lett.*, 95:086102(1–4), 2005. 5, 6, 11

[15] D. McLean. *Grain Boundaries in Metals*. Oxford Press, London, England, 1957. 40

[16] C. Nan and R. Birringer. Determining the kapitza resistance and the thermal conductivity of polycrystals: A simple model. *Phys. Rev. B*, 57:8264–8268, 1998. 28

[17] B. G. Orr, D. A. Kessler, C. W. Snyder, and L. M. Sander. A model for strain-induced roughening and coherent island growth. *Europhys. Lett.*, 19:33–38, 1992. 6, 12

[18] N. J. Petch. The cleavage strength of polycrystals. *J. Iron Steel Inst.*, 174:25–28, 1953. 28

[19] T. Radetic, C. Ophus, D.L. Olmsted, M. Asta, and U. Dahmen. Mechanism and dynamics of shrinking island grains in mazed bicrystal thin films of au. *Acta Mater.*, 60:7051–7063, 2012. ix, 2, 27, 40, 42

[20] G. Russo and P. Smereka. Computation of strained epitaxial growth in three dimensions by kinetic monte carlo. *J. Comput. Phys.*, 214:809–828, 2005. 5, 8

[21] T. P. Schulze. Efficient kinetic monte carlo simulation. *J. Comput. Phys.*, 227:2455–2462, 2008. 2

[22] T. P. Schulze and P. Smereka. An energy localization principle and its application to fast kinetic monte carlo simulation of heteroepitaxial growth. *J. Mech. Phys. Solids*, 57:521 – 538, 2009. 1, 5, 7, 11, 14, 45

[23] T. P. Schulze and P. Smereka. Simulation of three-dimensional strained heteroepitaxial growth using kinetic monte carlo. *Commun. Comput. Phys.*, 10:1089–1112, 2011. 6

[24] T. P. Schulze and P. Smereka. Kinetic monte carlo simulation of heteroepitaxial growth: Wetting layers, quantum dots, capping, and nanorings. *Phys. Rev. B*, 86:235313, 2012. 1, 5, 6

[25] B. J. Spencer, P. W. Voorhees, and S. H. Davis. Morphological instability in epitaxially strained dislocation-free solid films. *Phys. Rev. Lett.*, 67:3696–3699, 1991. 5

[26] D. J. Srolovitz, M. P. Anderson, G. S. Grest, and P. S. Sahni. Grain growth in two dimensions. *Scripta Metall.*, 17:241–246, 1983. ix, 29

[27] T. R. Tauchert. *Energy Principles in Structural Mechanics*. McGraw-Hill, New York, NY, 1974. 9

[28] V. Tikare, E. A. Holm, D. Fan, and L.-Q. Chen. Comparison of phase-field and potts models for coarsening processes. *Acta Metall.*, 47:363–371, 1999. 29

[29] M. Upmanyu, D. J. Srolovitz, A. E. Lobkovsky, J. A. Warren, and W. C. Carter. Simultaneous grain boundary migration and grain rotation. *Acta Mater.*, 54:1707–1719, 2006. 34

[30] A. F. Voter. *Introduction to the Kinetic Monte Carlo Method*. Springer, Dordrecht, Netherlands, 2007. Appeared in *Radiation Effects in Solids*, edited by K. E. Sickafus, E. A. Kotomin and B. P. Uberuaga, pp 1-23. 2

[31] H. Zhang, M. Upmanyu, and D. J. Srolovitz. Curvature driven grain boundary migration in aluminum: molecular dynamics simulations. *Acta Mater.*, 53:79–86, 2005. 28

Appendix

Appendix A

Derivation of (2.17)

We derive the solution to (2.16) by following the derivation provided by Landau and Lifshitz [13]. We begin by recalling (2.16):

$$\begin{aligned} \mu\Delta\mathbf{u} + (\lambda+\mu)\nabla(\nabla\cdot\mathbf{u}) &= \mathbf{0} \quad \text{for } z<0, && \text{(A.1)} \\ \widetilde{\mathbf{T}}\mathbf{e}_3 &= -\sigma_1\left(h_x(x,y)\mathbf{e}_1 + h_y(x,y)\mathbf{e}_2\right) \quad \text{at } z=0, && \text{(A.2)} \\ \mathbf{u} &\to \mathbf{0} \quad \text{as } |\mathbf{x}|\to\infty. \end{aligned}$$

We will seek a solution

$$\mathbf{u} = \mathbf{f} + \nabla\phi, \tag{A.3}$$

where ϕ is some scalar function and the vector $\mathbf{f}$ is harmonic. That is,

$$\Delta\mathbf{f} = \mathbf{0}.$$

Substituting (A.3) in (A.1), we obtain the following equation for ϕ:

$$\Delta\phi = -\frac{\lambda+\mu}{\lambda+2\mu}\nabla\cdot\mathbf{f}. \tag{A.4}$$

Let $\mathbf{f} = \langle f_1, f_2, f_3 \rangle$ and write the functions f_1 and f_2 as the z-derivative of some functions g_1 and g_2:

$$f_1 = \frac{\partial g_1}{\partial z}, \quad f_2 = \frac{\partial g_2}{\partial z}. \tag{A.5}$$

Since $\mathbf{f}$ is harmonic, we can choose the functions g_1 and g_2 to be harmonic:

$$\Delta g_1 = 0, \quad \Delta g_2 = 0.$$

Substituting (A.5) in (A.4), we have

$$\Delta\phi = -\frac{\lambda+\mu}{\lambda+2\mu}\frac{\partial}{\partial z}\left(\frac{\partial g_1}{\partial x} + \frac{\partial g_2}{\partial y} + f_3\right).$$

Since g_1, g_2 and f_3 are harmonic, it is easy to verify that a function ϕ that satisfies this equation can be written as

$$\phi = -\frac{(\lambda+\mu)z}{2(\lambda+2\mu)}\left(\frac{\partial g_1}{\partial x} + \frac{\partial g_2}{\partial y} + f_3\right) + \psi, \tag{A.6}$$

where ψ is another harmonic function. It follows from (A.3), (A.5) and (A.6) that the problem of finding the displacement field $\mathbf{u}$ reduces to that of finding the harmonic functions g_1, g_2, f_3 and ψ.

We now turn our attention to the boundary conditions which must be satisfied at the free surface. It follows from (A.2) that

$$\begin{cases} \widetilde{T}_{13} = -\sigma_1 h_x(x,y), \\ \widetilde{T}_{23} = -\sigma_1 h_y(x,y), \\ \widetilde{T}_{33} = 0. \end{cases}$$

It follows that

$$\begin{cases} \left[\frac{\partial^2 g_1}{\partial z^2}\right]_{z=0} + \left[\frac{\partial}{\partial x}\left\{\frac{\mu}{\lambda+2\mu}f_3 - \frac{\lambda+\mu}{\lambda+2\mu}\left(\frac{\partial g_1}{\partial x} + \frac{\partial g_2}{\partial y}\right) + 2\frac{\partial \psi}{\partial z}\right\}\right]_{z=0} = -\frac{\sigma_1 h_x}{\mu}, \\ \left[\frac{\partial^2 g_2}{\partial z^2}\right]_{z=0} + \left[\frac{\partial}{\partial y}\left\{\frac{\mu}{\lambda+2\mu}f_3 - \frac{\lambda+\mu}{\lambda+2\mu}\left(\frac{\partial g_1}{\partial x} + \frac{\partial g_2}{\partial y}\right) + 2\frac{\partial \psi}{\partial z}\right\}\right]_{z=0} = -\frac{\sigma_1 h_y}{\mu}, \end{cases} \tag{A.7}$$

and

$$\left[\frac{\partial}{\partial z}\left\{f_3 - \left(\frac{\partial g_1}{\partial x} + \frac{\partial g_2}{\partial y}\right) + 2\frac{\partial \psi}{\partial z}\right\}\right]_{z=0} = 0. \tag{A.8}$$

We note that the conditions (A.7) and (A.8) on g_1, g_2, f_3 and ψ do not uniquely determine them. Therefore, we can impose an additional condition on these quantities. A convenient choice is to set

$$\frac{\mu}{\lambda+2\mu}f_3 - \frac{\lambda+\mu}{\lambda+2\mu}\left(\frac{\partial g_1}{\partial x} + \frac{\partial g_2}{\partial y}\right) + 2\frac{\partial \psi}{\partial z} = 0. \tag{A.9}$$

With this choice, the boundary conditions given by (A.7) reduce to

$$\begin{cases} \left[\frac{\partial^2 g_1}{\partial z^2}\right]_{z=0} = -\frac{\sigma_1 h_x}{\mu}, \\ \left[\frac{\partial^2 g_2}{\partial z^2}\right]_{z=0} = -\frac{\sigma_1 h_y}{\mu}. \end{cases} \tag{A.10}$$

Then, equations (A.8)-(A.10) uniquely determine the functions g_1, g_2, f_3 and ψ.

At this point, we aim to find the Green's tensor for the equations of equilibrium of a semi-infinite medium. To this end, we consider the case in which the free surface of the medium is subjected to a concentrated force $\mathbf{F}$. That is, the force is applied to an area so small that it can be regarded as a point. Then, the surface forces are given by $\mathbf{P} = \mathbf{F}\delta(\mathbf{x})\delta(\mathbf{y})$, with the origin being the point of application of the force.

Using the method of images, it is easy to show that a harmonic function in the lower half-space that tends to zero at infinity with a prescribed Neumann boundary condition is given by the formula

$$g(x,y,z) = -\frac{1}{2\pi}\int_{-\infty}^{\infty}\int_{-\infty}^{\infty}\frac{\partial g}{\partial \nu}(x',y',0)\frac{dx'dy'}{r'},$$

where $r' = \sqrt{(x-x')^2 + (y-y')^2 + z^2}$ and $\frac{\partial}{\partial \nu}$ denotes the normal derivative. Since all of the quantities in braces in (A.8) are harmonic, it follows that

$$f_3 - \left(\frac{\partial g_1}{\partial x} + \frac{\partial g_2}{\partial y} \right) + 2 \frac{\partial \psi}{\partial z} = 0. \tag{A.11}$$

Furthermore, it follows from (A.10) that

$$\begin{aligned} \frac{\partial g_1}{\partial z} &= -\frac{1}{2\pi} \int_{-\infty}^{\infty} \int_{-\infty}^{\infty} -\frac{\sigma_1 h_x(x', y') \delta(x') \delta(y')}{\mu r'} dx' dy' = \frac{\sigma_1 h_x(0,0)}{2\pi \mu r}, \\ \frac{\partial g_2}{\partial z} &= -\frac{1}{2\pi} \int_{-\infty}^{\infty} \int_{-\infty}^{\infty} -\frac{\sigma_1 h_y(x', y') \delta(x') \delta(y')}{\mu r'} dx' dy' = \frac{\sigma_1 h_y(0,0)}{2\pi \mu r}, \end{aligned} \tag{A.12}$$

where $r = \sqrt{x^2 + y^2 + z^2}$.

In order to find ϕ, we need $\frac{\partial g_1}{\partial x}$ and $\frac{\partial g_2}{\partial y}$. It follows from (A.12) that

$$\frac{\partial^2 g_1}{\partial x \partial z} = -\frac{\sigma_1 h_x(0,0)}{2\pi\mu} \frac{x}{r^3}, \quad \frac{\partial^2 g_2}{\partial y \partial z} = -\frac{\sigma_1 h_y(0,0)}{2\pi\mu} \frac{y}{r^3}.$$

We now integrate both equations over z from $-\infty$ to z to obtain

$$\begin{aligned} \frac{\partial g_1}{\partial x} &= -\frac{\sigma_1 h_x(0,0)}{2\pi\mu} \frac{x}{r(r-z)}, \\ \frac{\partial g_2}{\partial y} &= -\frac{\sigma_1 h_y(0,0)}{2\pi\mu} \frac{y}{r(r-z)}. \end{aligned} \tag{A.13}$$

It follows from (A.9), (A.11) and (A.13) that

$$\begin{aligned} f_3 &= \frac{\mu}{\lambda + \mu} \left(\frac{\partial g_1}{\partial x} + \frac{\partial g_2}{\partial y} \right) \\ &= -\frac{\sigma_1}{2\pi(\lambda+\mu) r(r-z)} \left(h_x(0,0) x + h_y(0,0) y \right) \end{aligned} \tag{A.14}$$

and

$$\frac{\partial \psi}{\partial z} = -\frac{\lambda \sigma_1}{4\pi\mu(\lambda+\mu) r(r-z)} \left(h_x(0,0) x + h_y(0,0) y \right). \tag{A.15}$$

The only two remaining quantities to find are $\frac{\partial \psi}{\partial x}$ and $\frac{\partial \psi}{\partial y}$. To this end, we integrate (A.15) to find

$$\psi = -\frac{\lambda \sigma_1}{4\pi\mu(\lambda+\mu)} \left(\frac{h_x(0,0)x}{r-z} + \frac{h_y(0,0)y}{r-z} \right).$$

Then,

$$\begin{aligned} \frac{\partial \psi}{\partial x} &= \frac{\lambda \sigma_1}{4\pi\mu(\lambda+\mu)} \left(\frac{h_x(0,0)x^2 + h_y(0,0)xy}{r(r-z)^2} - \frac{h_x(0,0)}{r-z} \right) \\ \frac{\partial \psi}{\partial y} &= \frac{\lambda \sigma_1}{4\pi\mu(\lambda+\mu)} \left(\frac{h_x(0,0)xy + h_y(0,0)y^2}{r(r-z)^2} - \frac{h_y(0,0)}{r-z} \right). \end{aligned} \tag{A.16}$$

We now combine (A.3), (A.5), (A.6), (A.12), (A.13), (A.14), (A.15) and (A.16) to find the solution for the case of a point force:

$$\begin{cases} u_1 = -\frac{\sigma_1}{4\pi\mu} \left[h_x(0,0) \frac{-\frac{\lambda+2\mu}{\lambda+\mu} r + z}{r(r-z)} + (h_x(0,0)x + h_y(0,0)y) \frac{\left[r\left(-\frac{\lambda}{\lambda+\mu} r + 2z\right) - z^2 \right] x}{r^3 (r-z)^2} \right], \\ u_2 = -\frac{\sigma_1}{4\pi\mu} \left[h_y(0,0) \frac{-\frac{\lambda+2\mu}{\lambda+\mu} r + z}{r(r-z)} + (h_x(0,0)x + h_y(0,0)y) \frac{\left[r\left(-\frac{\lambda}{\lambda+\mu} r + 2z\right) - z^2 \right] y}{r^3 (r-z)^2} \right], \\ u_3 = -\frac{\sigma_1}{4\pi\mu} \left[(h_x(0,0)x + h_y(0,0)y) \left(\frac{\mu}{(\lambda+\mu) r(r-z)} - \frac{z}{r^3} \right) \right], \end{cases}$$

where $\mathbf{u} = \langle u_1, u_2, u_3 \rangle$. It follows that the solution to (2.16) is

$$u_i = \int_{-\infty}^{\infty} \int_{-\infty}^{\infty} G_{ik}(x - x', y - y', z) P_k(x', y') dx' dy',$$

where each component is summed over k, $\mathbf{G}$ is the Green's tensor given by

$$\mathbf{G} = \frac{\mathbf{1}}{4\pi\mu} \begin{bmatrix} \frac{-\frac{\lambda+2\mu}{\lambda+\mu} r + z}{r(r-z)} + \frac{\left[r\left(-\frac{\lambda}{\lambda+\mu} r + 2z\right) - z^2 \right] x^2}{r^3 (r-z)^2} & \frac{\left[r\left(-\frac{\lambda}{\lambda+\mu} r + 2z\right) - z^2 \right] xy}{r^3 (r-z)^2} & 0 \\ \frac{\left[r\left(-\frac{\lambda}{\lambda+\mu} r + 2z\right) - z^2 \right] xy}{r^3 (r-z)^2} & \frac{-\frac{\lambda+2\mu}{\lambda+\mu} r + z}{r(r-z)} + \frac{\left[r\left(-\frac{\lambda}{\lambda+\mu} r + 2z\right) - z^2 \right] y^2}{r^3 (r-z)^2} & 0 \\ x \left(\frac{\mu}{(\lambda+\mu) r(r-z)} - \frac{z}{r^3} \right) & y \left(\frac{\mu}{(\lambda+\mu) r(r-z)} - \frac{z}{r^3} \right) & 0 \end{bmatrix},$$

and $\mathbf{P}$ is the force distribution given by

$$\mathbf{P} = \begin{bmatrix} -\sigma_1 h_x(x,y) \\ -\sigma_1 h_y(x,y) \\ 0 \end{bmatrix}.$$

Integrating by parts and using the compact support of h, we have

$$u = \sigma_1 \int\int_{x'^2+y'^2 \leq R^2} \mathbf{f}(x-x', y-y', z) h(x', y')\ dx'dy',$$

where $\mathbf{f} = \frac{\partial}{\partial x}\mathbf{G}\mathbf{e}_1 + \frac{\partial}{\partial y}\mathbf{G}\mathbf{e}_2$.

Vita

Kyle Louis Golenbiewski was born in Jenison, MI, to the parents of Roy Joseph and Mary Alice Golenbiewski. He has one older brother by the name of Aaron Joseph. He attended Maplewood Elementary before moving on to Jenison Middle and High School. After graduation, he attended Grand Valley State University in Allendale, MI, where he graduated Magna Cum Laude with a Bachelor of Science degree in Mathematics and Physics. Looking to further pursue his interest in the mathematical sciences, he accepted a Graduate Teaching Assistantship in the mathematics department at the University of Tennessee, Knoxville. It was here that he developed a love for teaching and graduated with a Doctor of Philosophy degree in Mathematics. He has chosen to pursue his love of teaching and accepted a position as an Assistant Professor in the mathematics department at the University of North Alabama in Florence, AL.